Time-dependent density-functional calculations for the optical spectra of molecules, clusters, and nanocrystals



2003 J. Phys.: Condens. Matter 15 R1517

(http://iopscience.iop.org/0953-8984/15/35/201)

INSTITUTE OF PHYSICS PUBLISHING JOURNAL OF PHYSICS: CONDENSED MATTER

J. Phys.: Condens. Matter **15** (2003) R1517–R1547 PII: S0953-8984(03)33488-5

**TOPICAL REVIEW**

# Time-dependent density-functional calculations for the optical spectra of molecules, clusters, and nanocrystals

**James R Chelikowsky**[1], **Leeor Kronik**[2] **and Igor Vasiliev**[3]

[1] Department of Chemical Engineering and Materials Science, University of Minnesota, Minneapolis, MN 55455, USA
[2] Department of Materials and Interfaces, Weizmann Institute of Science, Rehovoth 76100, Israel
[3] Department of Physics, New Mexico State University, Las Cruces, NM 88003, USA

E-mail: jrc@msi.umn.edu, leeor.kronik@weizmann.ac.il and vasiliev@nmsu.edu

Received 18 June 2003
Published 22 August 2003
Online at stacks.iop.org/JPhysCM/15/R1517

**Abstract**

In this review, we will describe calculations using time-dependent density-functional theory (DFT) combined with pseudopotentials to determine excited state properties of matter. While a computational framework for ground state properties of condensed matter is well established, calculations for excited state properties are at a more formative stage. Time-dependent DFT represents an important advance by providing an explicit treatment of relevant correlation effects for electronic excitations. As such, it offers an *ab initio* formalism for excited states that avoids many of the drawbacks associated with empirical or semi-empirical methods. We will illustrate applications of time-dependent DFT to a variety of systems ranging from molecules and atomic clusters to quantum dots, which contain several hundred atoms.

(Some figures in this article are in colour only in the electronic version)

## Contents



  

## 1. Introduction

At confined dimensions, optical properties of matter are often altered. For example, elemental silicon possesses very different properties as a function of size. While silicon in its bulk form is the dominant material for making electronic devices, it has poor optical properties for optoelectronic devices such as solar cells or lasers. However, the poor optical properties of silicon in the bulk form can be dramatically altered at nanoscale dimensions: the bandgap in silicon can be blue-shifted from the infra-red to the optical region as a function of size. One of the first manifestations of this effect was observed in porous silicon, which exhibits remarkable room temperature luminescence [1, 2]. The localization of excitations to nanoscale dimensions is an essential attribute of porous silicon. This form of silicon could be a good optical material, if technological issues can be resolved.

To capitalize properly on such phenomena, a deeper understanding of the optical properties of matter will be required. Historically, optical properties have played a key role in our understanding of the electronic structure of matter, e.g., the first realistic energy band structures of semiconductors were found using optical properties as input into electronic structure calculations [3]. Unfortunately, optical excitations based on contemporary approaches can be especially challenging because most commonly used methods for structural energies, such as density-functional theory (DFT), are not well suited for excited state properties. The problem is exacerbated for nanoscale systems where the many body effects are enhanced by the physical confinement of the excitation and where hundreds or thousands of atoms are required to model the simplest systems.

Here we review some recent advances in computational methods for predicting the optical properties of materials at the nanoscale, or sub-nanoscale. Our focus is on utilizing the pseudopotential method along with DFT implemented with the local density approximation (LDA) [4–6]. The combination of the LDA and the pseudopotential approach has proved to be very successful for predicting the *structural and cohesive properties* of various solids [7–10]. The pseudopotential approximation removes the chemically inert core electrons from the problem, effectively reducing the number of electronic degrees of freedom in the quantum mechanical equations. Pseudo-wavefunctions are smoothly varying and can be easily represented within any chosen basis such as a plane wave representation or grid methods such as finite element or finite differencing [11]. For localized systems such as molecules or nanoclusters, a direct real-space implementation of this technique is particularly advantageous [11–20]. With this approach, the Kohn–Sham equation for electronic states is solved on a real-space three-dimensional grid within a spherical boundary domain. The kinetic energy operator is approximated by a higher-order finite difference expansion on grid points [21, 22]. Unlike 'supercell' calculations in momentum space [23], real-space methods do not produce an artificial periodicity, and do not impose restrictions on the net charge of the system.

The pseudopotential approximation is highly accurate and can be tested by explicitly including core states [7]. However, implementations of DFT can be more problematic. In principle, DFT is exact; however, in practice approximations must be made. One of the most significant limitations of 'conventional' density functional formalism is its inability to deal with electronic excitations. Within time-independent, or static, DFT, a quantum mechanical

system is described through the electronic charge density. While this approach can be accurate for the ground state of a many-electron system, the excited electronic states are not adequately represented by the static formalism [24, 25]. The inability to describe excitations severely restricts the range of applications for conventional density functional methods, since many important physical properties such as optical absorption and emission, response to time-dependent fields, the dynamical dielectric function and the bandgap in semiconductors are associated with excited states.

Explicit calculations for excited states can present enormous challenges for theoretical methods. Accurate calculations for excitation energies and absorption spectra typically require computationally intensive techniques, such as the configuration interaction method [26, 27], quantum Monte Carlo simulations [28–30] or the Green function methods [31–33]. While these methods describe electronic excitations properly, they are usually limited to very small systems because of high computational demands. For example, in quantum Monte Carlo methods numerous calls must made on the energy integrand and in Green function methods complex matrix elements must be evaluated.

An alternative approach is to consider methods based on time-dependent DFT such as those using the time-dependent local density approximation (TDLDA) [24, 25, 34–43]. The TDLDA technique can be viewed as a natural extension of the ground state density-functional LDA formalism, designed to include the proper representation of excited states. TDLDA excitation energies of a many-electron system are usually computed from conventional, time-independent Kohn–Sham transition energies and wavefunctions. Compared to other theoretical methods for excited states, the TDLDA technique requires considerably less computational effort; e.g., the computational load is often comparable to a static density functional calculation [44]. Despite its relative simplicity, the TDLDA method incorporates screening and relevant correlation effects for electronic excitations [24, 25, 34, 35]. In this sense, TDLDA represents a fully *ab initio* formalism for excited states.

We will review this technique by illustrating computations for transition energies and optical absorption spectra for several representative systems such as diatomic molecules, clusters and quantum dots. Our emphasis will be on real-space methods for the electronic structure problem and on frequency-domain methods for TDLDA. We note that other methods have been successfully implemented for TDLDA; they are discussed elsewhere [40–42, 45].

## 2. Theoretical methods

### *2.1. Finite difference pseudopotential method*

The first step in calculating the excited states is to extract the Kohn–Sham eigenvalues and orbitals for the static case. An efficacious approach for localized systems such as clusters and quantum dots is to use a real-space approach. Such approaches are often based on a higher-order finite difference pseudopotential method [12, 13]. The electronic problem is defined by the Kohn–Sham equation of the form

$$\left(-\frac{\nabla^2}{2} + \sum_a v_{\rm ion}^{\rm p}(\boldsymbol{r} - \boldsymbol{r}_a) + v_{\rm H}[\rho(\boldsymbol{r})] + v_{\rm xc}[\rho(\boldsymbol{r})]\right)\psi_i(\boldsymbol{r}) = \epsilon_i\psi_i(\boldsymbol{r}). \tag{1}$$

Atomic units, au ($\hbar = e = m = 1$), are used throughout unless otherwise specified. In equation (1), the all-electron potential of each ion at $\boldsymbol{r}_a$ is replaced by a pseudopotential $v_{\rm ion}^{\rm p}(\boldsymbol{r} - \boldsymbol{r}_a)$, which accounts for the interaction with core electrons and nuclei. The Hartree potential, $v_{\rm H}[\rho(\boldsymbol{r})]$, given by

$$\nabla^2 v_{\rm H}[\rho(\boldsymbol{r})] = -4\pi\rho(\boldsymbol{r}) \tag{2}$$

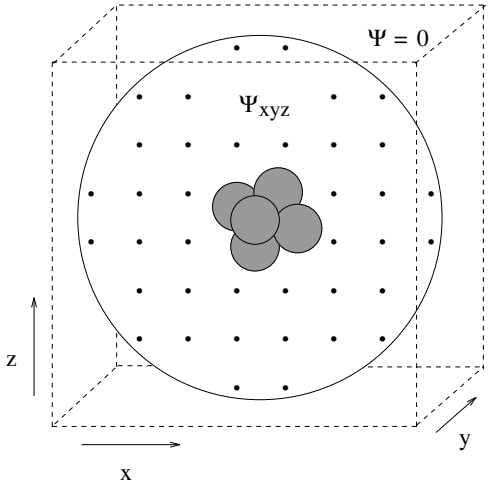


**Figure 1.** Schematic real-space grid for localized systems. The system of interest is placed in a spherical domain. Outside this domain, the wavefunctions vanish.

describes the electrostatic interactions among valence electrons, and the exchange–correlation potential, $v_{\rm xc}[\rho(\boldsymbol{r})]$, represents the non-classical part of the Hamiltonian. $\rho(\boldsymbol{r})$ is the charge density. The Kohn–Sham eigenvalues, $\epsilon_i$, and eigenwavefunctions, $\psi_i(\boldsymbol{r})$, can be used to extract the electronic properties of the system of interest.

In real-space methods, the potentials and electronic wavefunctions are set up on a grid. The grid can be a simple Cartesian three-dimensional grid within a spherical domain, as shown schematically in figure 1. Uniform grids are highly advantageous; they offer an unbiased representation and are easy to implement [12–19]. The grid points inside the sphere are described by their discrete space coordinates, $\{x, y, z\}$. Outside the boundary domain wavefunctions are required to vanish. The kinetic energy term, $-\nabla^2/2$, is approximated by a higher-order finite difference expansion for the Laplacian operator, which replaces spatial derivatives with a weighted sum of the wavefunction values at neighbouring grid points,

$$\nabla^2\psi_i(x, y, z) = \frac{1}{h^2}\sum_{n=-N}^{N} C_{N,n}^{\{2\}}\left[\psi_i(x+nh, y, z) + \psi_i(x, y+nh, z) + \psi_i(x, y, z+nh)\right] \qquad (3)$$

where $h$ is the grid spacing and $C_{N,n}^{\{2\}}$ are the coefficients in the order-$N$ finite difference expansion for the second derivative. The numerical values of the expansion coefficients are readily available in the literature [21, 22].

The finite difference order is usually chosen as a compromise between having a fine grid and a large but sparse Hamiltonian matrix, and having a coarse grid and a small but less sparse matrix. In electronic structure calculations, a finite difference expansion between $N = 4$ and 6 typically presents the optimum choice [12, 13].

The ionic pseudopotential is a nonlocal operator, which simulates the angular-momentum-dependent interaction between the valence electrons and the ion core. We employ the real-space version of the Kleinman–Bylander [46] form of the nonlocal pseudopotential,

$$v_{\rm ion}(\boldsymbol{r}-\boldsymbol{r}_a)\psi_i(\boldsymbol{r}) = v_{\rm local}(\boldsymbol{r}-\boldsymbol{r}_a)\psi_i(\boldsymbol{r}) + \sum_{l,m} G_{lm}\Delta v_l(\boldsymbol{r}-\boldsymbol{r}_a)\phi_{lm}(\boldsymbol{r}-\boldsymbol{r}_a) \qquad (4)$$

where $v_{\rm local}$ is the local ionic pseudopotential, $\Delta v_l = v_l - v_{\rm local}$ is the difference between the local potential and the potential component with the angular momentum $l$, $\phi_{lm}$ are the atomic

pseudo-wavefunctions, and the projection coefficients, $G_{lm}$, are calculated as

$$G_{lm} = \frac{\langle \phi_{lm} | \Delta v_l | \psi_i \rangle}{\langle \phi_{lm} | \Delta v_l | \phi_{lm} \rangle}. \tag{5}$$

This form of the pseudopotential limits the non-locality to a small region around each atom. All calculations presented in this review employed Troullier–Martins pseudopotentials [47].

The exchange–correlation potential within LDA is approximated by a local functional of the charge density. In our calculations, we used a parametrized form of the Ceperley–Alder functional [48–50]. Owing to the non-linear nature of the LDA exchange–correlation functional, the accuracy of this approximation can be improved by accounting for interactions between the valence charge density and the core charge density. The exchange–correlation potential is evaluated as a functional of the *core-corrected* charge density [51],

$$\rho(\boldsymbol{r}) = \rho_{\mathrm{v}}(\boldsymbol{r}) + \sum_a \rho_{\mathrm{core}}(|\boldsymbol{r} - \boldsymbol{r}_a|), \tag{6}$$

where $\rho_{\mathrm{core}}(|\boldsymbol{r} - \boldsymbol{r}_a|)$ is a fixed partial correction for the core charge density [51] and $\rho_{\mathrm{v}}(\boldsymbol{r})$ is the *valence* charge density calculated as

$$\rho_{\mathrm{v}}(\boldsymbol{r}) = -\sum_i n_i |\psi_i(\boldsymbol{r})|^2, \tag{7}$$

where $\psi_i(\boldsymbol{r})$ are single-electron wavefunctions and $n_i$ are occupation numbers.

The Hartree potential is obtained by setting up and solving the Poisson equation for the charge density using the conjugate-gradient method [52]. To solve the Poisson equation numerically, we use a higher-order finite difference expansion for the Laplacian operator, similar to one given by equation (3). Boundary conditions for points outside the main domain are determined by a multipole expansion of the charge density.

Within this framework, the off-diagonal elements of the Hamiltonian matrix are produced only by the kinetic energy and the nonlocal part of the ionic pseudopotential. All other terms, including the local part of the pseudopotential, the Hartree potential, and the exchange–correlation potential, contribute only to the main diagonal of the Hamiltonian. The system of Kohn–Sham equations for electronic states is solved within a self-consistent field. The initial charge density distribution is constructed by superposing atomic charge densities. Based on the initial charge density, we calculate the Hartree and exchange–correlation potentials, and set up the Hamiltonian matrix. The matrix equation is solved numerically by iterative diagonalization using the generalized Davidson algorithm [52, 53]. From the solution of this matrix equation we obtain a new distribution of the charge density. The self-consistent procedure is repeated until we achieve the desired convergence of the numerical solution. The convergence criterion in our calculations is defined by the root-mean-square difference between the input and output potentials. Typically, one requires this difference to be less than $10^{-4}$ au.

### *2.2. Time-dependent density functional theory*

The central theorem of DFT states that the external potential and the ground state energy of a system of interacting electrons are uniquely determined by the ground state charge density [4–6]. However, the traditional formulation of the density functional formalism is restricted to the *time-independent* case. A proper treatment of electronic excitations is not possible within the time-independent framework; it requires a generalization of DFT to time-dependent phenomena. This limitation has led to the development of *time-dependent* DFT (TDDFT) [54–62]. Within TDDFT, the main theorem of the density functional formalism is extended to time-dependent systems. Similarly to the case of time-independent DFT, the

time-dependent formalism reduces the many-electron problem to a set of self-consistent single-particle equations [59, 60],

$$\left(-\frac{\nabla^2}{2} + v_{\rm eff}[\rho(\boldsymbol{r},t)]\right)\psi_i(\boldsymbol{r},t) = \mathrm{i}\frac{\partial}{\partial t}\psi_i(\boldsymbol{r},t). \tag{8}$$

In this case, the single-particle wavefunctions, $\psi_i(\boldsymbol{r},t)$, and the effective potential, $v_{\rm eff}[\rho(\boldsymbol{r},t)]$, explicitly depend on time. The effective potential is given by

$$v_{\rm eff}[\rho(\boldsymbol{r},t)] = \sum_a v^{\rm p}_{\rm ion}(\boldsymbol{r}-\boldsymbol{r}_a) + v_{\rm H}[\rho(\boldsymbol{r},t)] + v_{\rm xc}[\rho(\boldsymbol{r},t)]. \tag{9}$$

The three terms on the right-hand side of equation (9) describe the external ionic potential, the Hartree potential, and the exchange–correlation potential, respectively. In the adiabatic approximation, which is local in *time*, the exchange–correlation potential and its first derivative can be expressed in terms of the *time-independent* exchange–correlation energy, $E_{\rm xc}[\rho]$,

$$v_{\rm xc}[\rho(\boldsymbol{r},t)] \simeq \frac{\delta E_{\rm xc}[\rho]}{\delta\rho(\boldsymbol{r})}, \qquad \frac{\delta v_{\rm xc}[\rho(\boldsymbol{r},t)]}{\delta\rho(\boldsymbol{r}',t')} \simeq \delta(t-t')\frac{\delta^2 E_{\rm xc}[\rho]}{\delta\rho(\boldsymbol{r})\delta\rho(\boldsymbol{r}')}. \tag{10}$$

The energy $E_{\rm xc}[\rho]$ in equation (10) can be further approximated by a regular LDA exchange–correlation functional:

$$E_{\rm xc}[\rho] = \int \rho(\boldsymbol{r})\epsilon_{\rm xc}[\rho(\boldsymbol{r})]\,\mathrm{d}\boldsymbol{r}. \tag{11}$$

The LDA makes a separate local approximation; i.e., within the LDA, the exchange–correlation energy density is local in *space*.

While the LDA in time-dependent DFT has proven itself for molecules, clusters, and small quantum dots and small clusters, several questions remain as areas of active research. The application of TDLDA to large, extended systems remains problematic. It is widely accepted that TDLDA as outlined here will approach the LDA results for extended systems and, consequently suffer the flaws of LDA such as exhibiting bandgaps much smaller than experiment [45]. However, recent work using modified forms of TDLDA suggest that it may be of use for extended systems [63, 64]. Also, most implementations of time-dependent DFT are based on the local density approximation or the generalized gradient approximation [65, 66]. However, these approximations are known to have the wrong asymptotic behaviour; e.g. the potential does not scale as $1/r$ for large distances. It is believed that more accurate TDLDA methods will necessitate other forms of the density functional. Examples of such an approach are the asymptotically corrected local density approximations introduced by Casida and Salahub [67], and by van Leeuwen and Baerends [68]. These potentials have recently been investigated using the current formalism [69].

### *2.3. Linear response in TDDFT*

The linear response formalism within TDDFT provides a theoretical basis for the TDLDA method. In this section, we illustrate how TDLDA excitation energies and oscillator strengths are derived from single-electron Kohn–Sham eigenvalues and eigenwavefunctions. A comprehensive analysis of time-dependent density-functional response theory can be found elsewhere [24, 25, 34, 35]. We use the general notation and follow the discussion of Casida [34, 35].

The response of the Kohn–Sham density matrix within TDDFT is obtained by introducing a time-dependent perturbation $\delta v_{\rm appl}(\boldsymbol{r},t)$. Due to the self-consistent nature of the Kohn–Sham Hamiltonian, the *effective* perturbation includes the response of the self-consistent field, $\delta v_{\rm SCF}[\rho(\boldsymbol{r},t)]$,

$$\delta v_{\rm eff}[\rho(\boldsymbol{r},t)] = \delta v_{\rm appl}(\boldsymbol{r},t) + \delta v_{\rm SCF}[\rho(\boldsymbol{r},t)], \tag{12}$$

where the self-consistent field is given by the last two terms in equation (9):

$$v_{\mathrm{SCF}}[\rho(\boldsymbol{r},t)] = \int \frac{\rho_{\mathrm{v}}(\boldsymbol{r}',t)}{|\boldsymbol{r}-\boldsymbol{r}'|}\,\mathrm{d}\boldsymbol{r}' + v_{\mathrm{xc}}[\rho(\boldsymbol{r},t)]. \tag{13}$$

With the frequency domain, the response of the Kohn–Sham density matrix, $\delta\boldsymbol{P}(\omega)$, to the perturbation can be derived using a generalized susceptibility, $\chi(\omega)$. For quasi-independent Kohn–Sham particles, the sum-over-states representation of the generalized susceptibility is given by

$$\chi_{ij\sigma,kl\tau}(\omega) = \delta_{i,k}\delta_{j,l}\delta_{\sigma,\tau}\frac{\lambda_{lk\tau}}{\omega-\omega_{lk\tau}}, \tag{14}$$

where $\lambda_{lk\tau} = n_{l\tau} - n_{k\tau}$ is the difference between the occupation numbers, and $\omega_{lk\tau} = \epsilon_{k\tau} - \epsilon_{l\tau}$ is the difference between the eigenvalues of the $l$th and $k$th single-particle states. The susceptibility in equation (14) is expressed in the basis of the unperturbed Kohn–Sham orbitals $\{\psi_{i\sigma}\}$ and the indices $i$, $j$, and $\sigma$ ($k$, $l$, and $\tau$) refer to space and spin wave components, respectively. The linear response of the density matrix is

$$\delta P_{ij\sigma}(\omega) = \sum_{kl\tau}\chi_{ij\sigma,kl\tau}(\omega)\delta v^{\mathrm{eff}}_{kl\tau}(\omega) = \frac{\lambda_{ji\sigma}}{\omega-\omega_{ji\sigma}}[\delta v^{\mathrm{appl}}_{ij\sigma}(\omega) + \delta v^{\mathrm{SCF}}_{ij\sigma}(\omega)]. \tag{15}$$

Equation (15) is, however, complicated by the fact that $\delta v_{\mathrm{SCF}}(\omega)$ depends on the response of the density matrix,

$$\delta v^{\mathrm{SCF}}_{ij\sigma}(\omega) = \sum_{kl\tau} K_{ij\sigma,kl\tau}\delta P_{kl\tau}(\omega), \tag{16}$$

where the coupling matrix $\boldsymbol{K}$ describes the response of the self-consistent field to changes in the charge density. Within the adiabatic approximation, this matrix is frequency independent. The analytical expression for the adiabatic coupling matrix, $K_{ij\sigma,kl\tau} = \partial v^{\mathrm{SCF}}_{ij\sigma}/\partial P_{kl\tau}$, can be derived from equation (13) by making use of the functional chain rule,

$$K_{ij\sigma,kl\tau} = \int\int \psi^*_{i\sigma}(\boldsymbol{r})\psi_{j\sigma}(\boldsymbol{r})\left(\frac{1}{|\boldsymbol{r}-\boldsymbol{r}'|} + \frac{\delta^2 E_{\mathrm{xc}}[\rho]}{\delta\rho_\sigma(\boldsymbol{r})\delta\rho_\tau(\boldsymbol{r}')}\right)\psi_{k\tau}(\boldsymbol{r}')\psi^*_{l\tau}(\boldsymbol{r}')\,\mathrm{d}\boldsymbol{r}\,\mathrm{d}\boldsymbol{r}'. \tag{17}$$

The functional derivative in equation (17) is evaluated with respect to the *unperturbed* charge densities. By using the coupling matrix, equation (15) can be rewritten as

$$\sum_{kl\tau}^{\lambda_{kl\tau}\neq 0}\left[\delta_{i,k}\delta_{j,l}\delta_{\sigma,\tau}\frac{\omega-\omega_{lk\tau}}{\lambda_{lk\tau}} - K_{ij\sigma,kl\tau}\right]\delta P_{kl\tau}(\omega) = \delta v^{\mathrm{appl}}_{ij\sigma}(\omega). \tag{18}$$

Since the summation in equation (18) is performed over all occupied and unoccupied orbitals, it contains both the particle–hole and hole–particle contributions [34, 35]. These contributions can be written as two separate equations: the particle–hole part of $v_{\mathrm{appl}}(\omega)$ is given by

$$\sum_{kl\tau}^{\lambda_{kl\tau}>0}\left[\delta_{i,k}\delta_{j,l}\delta_{\sigma,\tau}\frac{\omega-\omega_{lk\tau}}{\lambda_{lk\tau}} - K_{ij\sigma,kl\tau}\right]\delta P_{kl\tau}(\omega) - \sum_{kl\tau}^{\lambda_{kl\tau}>0} K_{ij\sigma,lk\tau}\delta P_{lk\tau}(\omega) = \delta v^{\mathrm{appl}}_{ij\sigma}(\omega) \tag{19}$$

and the hole–particle part of $v_{\mathrm{appl}}(\omega)$ is

$$\sum_{kl\tau}^{\lambda_{kl\tau}>0}\left[\delta_{i,k}\delta_{j,l}\delta_{\sigma,\tau}\frac{\omega-\omega_{lk\tau}}{\lambda_{lk\tau}} - K_{ji\sigma,lk\tau}\right]\delta P_{lk\tau}(\omega) - \sum_{kl\tau}^{\lambda_{kl\tau}>0} K_{ji\sigma,kl\tau}\delta P_{kl\tau}(\omega) = \delta v^{\mathrm{appl}}_{ji\sigma}(\omega). \tag{20}$$

Combining equations (19) and (20), one can separate the real and imaginary parts of the density matrix response, $\delta\boldsymbol{P}(\omega)$. If the basis functions $\{\psi_{i\sigma}\}$ in equation (17) are real, the coupling matrix $\boldsymbol{K}$ is also real and symmetric with respect to the interchange of space indices $i \leftrightarrow j$

and $k \leftrightarrow l$. Since $\delta \boldsymbol{P}(\omega)$ is Hermitian (i.e. $\delta P_{ji\sigma} = \delta P^*_{ij\sigma}$), the real part of $\delta \boldsymbol{P}(\omega)$ for a real perturbation $v_{\rm appl}(\omega)$ is given by

$$\sum_{kl\tau}^{\lambda_{kl\tau}>0} \left[ \frac{\delta_{i,k}\delta_{j,l}\delta_{\sigma,\tau}}{\lambda_{kl\tau}\omega_{kl\tau}}(\omega^2 - \omega^2_{kl\tau}) - 2K_{ij\sigma,kl\tau} \right] \mathrm{Re}(\delta P_{kl\tau})(\omega) = \delta v^{\rm appl}_{ij\sigma}(\omega), \qquad (21)$$

where $\mathrm{Re}(\delta P_{ij\sigma})(\omega)$ denotes the Fourier transform of the *real* part of $\delta P_{ij\sigma}(t)$.

Equation (21) can be used to obtain the density functional expression for the dynamic polarizability. This is accomplished by introducing a perturbation $\delta \hat{v}_{\rm appl}(t) = \hat{\gamma}\mathcal{E}_\gamma(t)$, where $\mathcal{E}_\gamma$ is an external electric field applied along the $\gamma$-axis, $\gamma = \{x, y, z\}$. The linear response of the dipole moment, $\delta\mu(\omega)$, is expressed through the real part of $\delta \boldsymbol{P}(\omega)$ as

$$\delta\mu_\beta(\omega) = -2 \sum_{ij\sigma}^{\lambda_{ij\sigma}>0} \beta_{ji\sigma}\, \mathrm{Re}(\delta P_{ij\sigma})(\omega), \qquad \beta = \{x, y, z\}. \qquad (22)$$

The components of the dynamic polarizability tensor are given by

$$\alpha_{\beta\gamma}(\omega) = \frac{\delta\mu_\beta(\omega)}{\mathcal{E}_\gamma(\omega)} = -\frac{2}{\mathcal{E}_\gamma(\omega)} \sum_{ij\sigma}^{\lambda_{ij\sigma}>0} \beta_{ji\sigma}\, \mathrm{Re}(\delta P_{ij\sigma})(\omega), \qquad \beta, \gamma = \{x, y, z\}. \qquad (23)$$

Solving equation (21) with respect to $\mathrm{Re}(\delta P_{ij\sigma})(\omega)$ and substituting the result into equation (23), one obtains the following matrix equation for the polarizability components:

$$\alpha_{\beta\gamma}(\omega) = 2\hat{\beta}\boldsymbol{R}^{1/2}[\boldsymbol{Q} - \omega^2\mathbf{1}]^{-1}\boldsymbol{R}^{1/2}\hat{\gamma}, \qquad \beta, \gamma = \{x, y, z\}, \qquad (24)$$

where the matrices $\boldsymbol{R}$ and $\boldsymbol{Q}$ are given by

$$R_{ij\sigma,kl\tau} = \delta_{i,k}\delta_{j,l}\delta_{\sigma,\tau}\lambda_{kl\tau}\omega_{kl\tau}, \qquad (25)$$

$$Q_{ij\sigma,kl\tau} = \delta_{i,k}\delta_{j,l}\delta_{\sigma,\tau}\omega^2_{kl\tau} + 2\sqrt{\lambda_{ij\sigma}\omega_{ij\sigma}}K_{ij\sigma,kl\tau}\sqrt{\lambda_{kl\tau}\omega_{kl\tau}}. \qquad (26)$$

The TDLDA expressions for excitation energies and oscillator strengths can be derived by comparing equation (24) with the general sum-over-states formula for the average dynamic polarizability, $\langle\alpha(\omega)\rangle = \mathrm{tr}(\alpha_{\beta\gamma}(\omega))/3 = \sum_I f_I/(\Omega_I^2 - \omega^2)$. The true excitation energies, $\Omega_I$, which correspond to the *poles* of the dynamic polarizability, are obtained from the solution of the eigenvalue problem,

$$\boldsymbol{Q}\boldsymbol{F}_I = \Omega_I^2\boldsymbol{F}_I. \qquad (27)$$

The oscillator strengths, $f_I$, which correspond to the *residues* of the dynamic polarizability, are given by

$$f_I = \tfrac{2}{3}\sum_{\beta=1}^{3} |\boldsymbol{B}_\beta^{\rm T}\boldsymbol{R}^{1/2}\boldsymbol{F}_I|^2, \qquad (28)$$

where $\boldsymbol{F}_I$ are the eigenvectors of equation (27), $(B_\beta)_{ij\sigma} = \int \psi^*_{i\sigma} r_\beta \psi_{j\sigma}\, \mathrm{d}\boldsymbol{r}$, and $\{r_1, r_2, r_3\} = \{x, y, z\}$.

### *2.4. Real-space implementation*

The adiabatic TDLDA calculations for optical spectra require only the knowledge of the time-independent single-electron Kohn–Sham transition energies and wavefunctions. The most computationally demanding part in such calculations is the evaluation of the coupling matrix given by equation (17). This equation can be split into two parts: $\boldsymbol{K} = \boldsymbol{K}^{(\rm I)} + \boldsymbol{K}^{(\rm II)}$. The first term represents a double integral over $1/|\boldsymbol{r} - \boldsymbol{r}'|$. Instead of performing the costly double

integration by direct summation, we calculate this term by solving the Poisson equation within the boundary domain. We employ the conjugate-gradient method to solve

$$\nabla^2 \Phi_{ij\sigma}(\boldsymbol{r}) = -4\pi \psi_{i\sigma}(\boldsymbol{r})\psi_{j\sigma}(\boldsymbol{r}). \tag{29}$$

The first term in equation (17) is calculated as

$$K^{(\mathrm{I})}_{ij\sigma,kl\tau} = \int \Phi_{ij\sigma}(\boldsymbol{r})\psi_{k\tau}(\boldsymbol{r})\psi_{l\tau}(\boldsymbol{r})\,\mathrm{d}\boldsymbol{r}. \tag{30}$$

The Poisson equation method provides a considerable speed-up as compared to the direct summation. The second term in equation (17) represents a double integral over the functional derivative of the exchange–correlation energy, $\delta^2 E_{\mathrm{xc}}[\rho]/\delta\rho_\sigma(\boldsymbol{r})\delta\rho_\tau(\boldsymbol{r}')$. Within the *local* approximation of the exchange–correlation potential this term is reduced to a single integral,

$$K^{(\mathrm{II})}_{ij\sigma,kl\tau} = \int \psi_{i\sigma}(\boldsymbol{r})\psi_{j\sigma}(\boldsymbol{r})\frac{\delta^2 E_{\mathrm{xc}}[\rho]}{\delta\rho_\sigma(\boldsymbol{r})\delta\rho_\tau(\boldsymbol{r})}\psi_{k\tau}(\boldsymbol{r})\psi_{l\tau}(\boldsymbol{r})\,\mathrm{d}\boldsymbol{r}, \tag{31}$$

where the LDA exchange–correlation energy, $E_{\mathrm{xc}}[\rho]$, is given by equation (11).

Equation (31) requires the evaluation of the second derivatives for the LDA exchange–correlation energy with respect to spin-up and spin-down charge densities. The LDA *exchange* energy per particle is normally approximated by that of the homogeneous electron gas [70],

$$\epsilon_{\mathrm{x}}[\rho_\sigma(\boldsymbol{r})] = -\frac{3}{4\pi}(6\pi^2\rho_\sigma(\boldsymbol{r}))^{1/3}, \qquad \sigma = \{\uparrow,\downarrow\}. \tag{32}$$

The first derivative of the total exchange energy determines the LDA exchange potential,

$$\frac{\delta E_{\mathrm{x}}[\rho]}{\delta\rho_\sigma} = v_{\mathrm{x}}[\rho_\sigma] = -\frac{1}{\pi}(6\pi^2\rho_\sigma)^{1/3}, \qquad \sigma = \{\uparrow,\downarrow\}. \tag{33}$$

The second derivatives are

$$\frac{\delta^2 E_{\mathrm{x}}[\rho]}{\delta\rho_\uparrow\delta\rho_\uparrow} = -\left(\frac{2}{9\pi}\right)^{1/3}\rho_\uparrow^{-2/3}, \qquad \frac{\delta^2 E_{\mathrm{x}}[\rho]}{\delta\rho_\uparrow\delta\rho_\downarrow} = 0. \tag{34}$$

We employ a parametrized form of Ceperley–Alder functional [48–50] for the LDA *correlation* energy. This functional is based on two different analytical expressions for $r_{\mathrm{s}} < 1$ and $r_{\mathrm{s}} \geqslant 1$, where $r_{\mathrm{s}} = (3/4\pi\rho)^{1/3}$ is the local Seitz radius and $\rho = \rho_\uparrow + \rho_\downarrow$. One can adjust the parametrization for $r_{\mathrm{s}} < 1$ to guarantee a continuous second derivative of the correlation energy. The adjusted interpolation formula for the correlation energy per particle is given by [71]

$$\epsilon_{\mathrm{c}}^{\mathrm{U,P}} = \begin{cases} A\ln r_{\mathrm{s}} + B + Cr_{\mathrm{s}}\ln r_{\mathrm{s}} + Dr_{\mathrm{s}} + Xr_{\mathrm{s}}^2\ln r_{\mathrm{s}}, & r_{\mathrm{s}} < 1 \\ \gamma/(1+\beta_1\sqrt{r_{\mathrm{s}}} + \beta_2 r_{\mathrm{s}}), & r_{\mathrm{s}} \geqslant 1, \end{cases} \tag{35}$$

where two separate sets of coefficients are used for the *polarized spin* (P) and *unpolarized spin* (U) cases. The numerical values of all fitting parameters appearing in equation (35) can be found in [72]. The adjusted interpolation formula for the correlation energy is continuous up to its second derivative, while the original Perdew–Zunger parametrization is not [50].

Equations (32)–(35) describe only the cases of the completely polarized and unpolarized spin. For intermediate spin polarizations, the correlation energy can be obtained with a simple interpolation formula,

$$\epsilon_{\mathrm{c}} = \epsilon_{\mathrm{c}}^{\mathrm{U}} + \xi(\rho)[\epsilon_{\mathrm{c}}^{\mathrm{P}} - \epsilon_{\mathrm{c}}^{\mathrm{U}}], \tag{36}$$

where

$$\xi(\rho) = \frac{1}{1-2^{-1/3}}(x_\uparrow^{4/3} + x_\downarrow^{4/3} - 2^{-1/3}); \qquad x_\uparrow = \frac{\rho_\uparrow}{\rho}, \quad x_\downarrow = \frac{\rho_\downarrow}{\rho}. \tag{37}$$

The expression for the second derivative of the correlation energy in the case of an arbitrary spin polarization can be written as

$$\frac{\delta^2 E_c[\rho]}{\delta\rho_\sigma \delta\rho_\tau} = \frac{\delta^2 E_c^U}{\delta\rho^2} + \xi(\rho)\left(\frac{\delta^2 E_c^P}{\delta\rho^2} - \frac{\delta^2 E_c^U}{\delta\rho^2}\right) + \left(\frac{\partial\xi(\rho)}{\partial\rho_\sigma} + \frac{\partial\xi(\rho)}{\partial\rho_\tau}\right)\left(\frac{\delta E_c^P}{\delta\rho} - \frac{\delta E_c^U}{\delta\rho}\right) + \frac{\partial^2\xi(\rho)}{\partial\rho_\sigma\partial\rho_\tau}\rho(\epsilon_c^P - \epsilon_c^U), \qquad \sigma,\tau = \{\uparrow,\downarrow\}, \tag{38}$$

where the spin polarization function, $\xi(\rho)$, and its derivatives are given by

$$\frac{\partial\xi(\rho)}{\partial\rho_\uparrow} = \frac{4}{3\rho(1-2^{-1/3})}(x_\uparrow^{1/3} - x_\uparrow^{4/3} - x_\downarrow^{4/3}), \tag{39}$$

$$\frac{\partial^2\xi(\rho)}{\partial\rho_\uparrow\partial\rho_\uparrow} = \frac{4}{9\rho^2(1-2^{-1/3})}(x_\uparrow^{-2/3} - 8x_\uparrow^{1/3} + 7(x_\uparrow^{4/3} + x_\downarrow^{4/3})), \tag{40}$$

$$\frac{\partial^2\xi(\rho)}{\partial\rho_\uparrow\partial\rho_\downarrow} = \frac{4}{9\rho^2(1-2^{-1/3})}(7(x_\uparrow^{4/3} + x_\downarrow^{4/3}) - 4(x_\uparrow^{1/3} + x_\downarrow^{1/3})). \tag{41}$$

### *2.5. Systems with unpolarized spin*

The TDLDA formalism presented in previous sections can be further simplified for systems with unpolarized spin. In this case, the spin-up and spin-down charge densities are equal, $\rho_\uparrow = \rho_\downarrow$, and equations (37) and (39)–(41) yield

$$\begin{aligned} &\xi(\rho) = 0, \qquad && \frac{\partial^2\xi(\rho)}{\partial\rho_\uparrow\partial\rho_\uparrow} = \frac{4}{9\rho^2(2^{1/3}-1)}, \\ &\frac{\partial\xi(\rho)}{\partial\rho_\uparrow} = 0, \qquad && \frac{\partial^2\xi(\rho)}{\partial\rho_\uparrow\partial\rho_\downarrow} = -\frac{4}{9\rho^2(2^{1/3}-1)}. \end{aligned} \tag{42}$$

Since the coordinate parts of spin-up and spin-down Kohn–Sham wavefunctions for systems with unpolarized spin are identical, $\psi_{i\uparrow} = \psi_{i\downarrow}$, it follows that $Q_{ij\uparrow,kl\uparrow} = Q_{ij\downarrow,kl\downarrow}$ and $Q_{ij\uparrow,kl\downarrow} = Q_{ij\downarrow,kl\uparrow}$. This allows us to separate 'singlet' and 'triplet' transitions by representing equation (27) in the basis set of $\{\boldsymbol{F}_+, \boldsymbol{F}_-\}$, chosen as

$$F_{ij}^{\{+,-\}} = \frac{1}{\sqrt{2}}(F_{ij\uparrow} \pm F_{ij\downarrow}). \tag{43}$$

In this basis, the matrix $\boldsymbol{Q}$ becomes

$$Q_{ij,kl}^{\{+,-\}} = \delta_{i,k}\delta_{j,l}\omega_{kl}^2 + 2\sqrt{\lambda_{ij}\omega_{ij}}K_{ij,kl}^{\{+,-\}}\sqrt{\lambda_{kl}\omega_{kl}}, \tag{44}$$

where $K_{ij,kl}^{\{+,-\}} = K_{ij\uparrow,kl\uparrow} \pm K_{ij\uparrow,kl\downarrow}$. The components of $\boldsymbol{K}^{\{+,-\}}$ in their explicit form are given by

$$K_{ij,kl}^{+} = 2\int\int \frac{\psi_i(\boldsymbol{r})\psi_j(\boldsymbol{r})\psi_k(\boldsymbol{r}')\psi_l(\boldsymbol{r}')}{|\boldsymbol{r}-\boldsymbol{r}'|}\,\mathrm{d}\boldsymbol{r}\,\mathrm{d}\boldsymbol{r}' + 2\int \psi_i(\boldsymbol{r})\psi_j(\boldsymbol{r})\left(\frac{\delta^2 E_c^U}{\delta\rho^2} - \frac{1}{(9\pi)^{1/3}\rho^{2/3}}\right)\psi_k(\boldsymbol{r})\psi_l(\boldsymbol{r})\,\mathrm{d}\boldsymbol{r}, \tag{45}$$

$$K_{ij,kl}^{-} = 2\int \psi_i(\boldsymbol{r})\psi_j(\boldsymbol{r})\left(\frac{4(\epsilon_c^P - \epsilon_c^U)}{9(2^{1/3}-1)} - \frac{1}{(9\pi)^{1/3}\rho^{2/3}}\right)\psi_k(\boldsymbol{r})\psi_l(\boldsymbol{r})\,\mathrm{d}\boldsymbol{r}. \tag{46}$$

For most practical applications, only 'singlet' transitions represented by the $\boldsymbol{F}_+$ basis vectors are of interest. Triplet transitions described by the $\boldsymbol{F}_-$ vectors have zero dipole oscillator strength and do not contribute to optical absorption [34, 35]. By solving equation (27) for the $\boldsymbol{F}_+$ vectors

only, we reduce the dimension of the eigenvalue problem by a factor of two. Equations (44)–(46), however, can only be applied to systems with unpolarized spin. In the case of an arbitrary spin polarization, the general form of the matrix $\boldsymbol{Q}$ presented by equation (26) with the coupling matrix given by equation (17) and the functional derivatives given by equations (33)–(41) must be used.

Other than the adiabatic local density approximation, no additional approximations have been made. The exact solution of the matrix equation (27) incorporates all relevant correlations among single-particle transitions.

The frequency-domain approach presented here lends itself naturally to a massively parallel solution within the real-space grid method. We use a multipole expansion to form the boundary condition, followed by a conjugate-gradient based solution, just as we did to evaluate the Hartree term in the time-independent Kohn–Sham (equation (1)). This step is the most computationally intensive step in forming the TDLDA matrix. However, each $ij\sigma$ combination defines a row in the coupling matrix and the $\psi_{ij\sigma}$ term of equation (3) is fixed within each row, so this need be done only once per matrix row. One merely evaluates the integrals of equations (30) and (31) as simple sums, for each element within a matrix row. The evaluation of each matrix row is completely independent of the evaluation of another row, leading to 'embarrassingly simple' parallelization, i.e. there is no need for communication between processors working on different matrix rows. Once, the matrix is diagonalized using any off-the-shelf diagonalization approach. Further implementation details can be found elsewhere [44].

## 3. Applications of time-dependent density-functional theory

### *3.1. Molecular systems*

The TDLDA can easily be applied to molecular systems such as simple dimers. These systems have two distinct advantages.

(1) They are sufficiently small to be handled by a variety of techniques. This allows one to compare methods with TDLDA. For example, the chemistry literature contains a number of papers where TDLDA or some variation thereof is applied to molecular systems; see e.g. [37–39].
(2) Experimental data exist for these systems, which allows us to compare the accuracy of the various approaches. Here we illustrate TDLDA applied to BeO and CO molecules.

We compare to experiment and to the GW–Bethe–Salpeter (GW–BS) method. The GW–BS method is a highly successful approach for predicting the optical properties of matter. The first step within this method is to consider a solution for a quasiparticle excitation [31–33, 73–75]. The energies and wavefunctions, $E^{\mathrm{QP}}$ and $\psi^{\mathrm{QP}}$ of quasiparticle excited states are obtained from a Dyson equation:

$$[T + V_{\mathrm{ext}}(\boldsymbol{r}) + V_{\mathrm{H}}(\boldsymbol{r})]\psi^{\mathrm{QP}}(\boldsymbol{r}) + \int \Sigma(\boldsymbol{r}, \boldsymbol{r}'; E^{\mathrm{QP}})\psi^{\mathrm{QP}}(\boldsymbol{r}')\,\mathrm{d}\boldsymbol{r}' = E^{\mathrm{QP}}\psi^{\mathrm{QP}}(\boldsymbol{r}) \tag{47}$$

where $T$ is the kinetic energy operator, $V_{\mathrm{ext}}$ is the external potential from the ion cores (in our case this corresponds to the ionic pseudopotential), $V_{\mathrm{H}}$ is the Hartree potential, and $\Sigma$ is the electron self-energy operator. Equation (47) is similar in form to equation (1), save for the physical content of the terms. Evaluating the quasiparticle term $\Sigma$ is considerably more difficult than the eigenvalue problem in equation (1). $\Sigma$ is a nonlocal, energy-dependent, non-Hermitian operator whose imaginary part gives the lifetime of the excitation [31–33, 73–75].

The GW approximation to a solution of equation (47) involves constructing the self-energy operator as the first-order term in a series expansion of the screened Coulomb interaction, $W$, and the dressed Green function, $G$, of the electron:

$$\Sigma(\boldsymbol{r}, \boldsymbol{r}'; E^{\mathrm{QP}}) = \frac{\mathrm{i}}{2\pi} \int \mathrm{d}\omega \, \mathrm{e}^{-\mathrm{i}\delta\omega} G(\boldsymbol{r}, \boldsymbol{r}'; E - \omega) W(\boldsymbol{r}, \boldsymbol{r}'; \omega) \tag{48}$$

where $\delta$ is a positive infinitesimal. $W = \epsilon^{-1} V_{\mathrm{c}}$ where $\epsilon$ is the dielectric response function and $V_{\mathrm{c}}$ is the bare Coulomb interaction. This term contains the dynamical many-body effects for electron–electron interactions. The heart of this approach concerns an accurate description of the dielectric response function: $\epsilon(\boldsymbol{r}, \boldsymbol{r}'; \omega)$. In crystalline matter, a dielectric function is constructed in reciprocal space: $\epsilon_{\vec{G},\vec{G}'}(\vec{q}, \omega)$. This function contains 'local field' effects, i.e., it contains variations of the electronic screening within the unit cell.

The strategy for solving equation (47) involves using LDA wavefunctions for the quasiparticles and constructing a dielectric matrix [31–33, 73–75]. Once the GW part of the problem is solved, it is possible to include the electron–hole interaction component. We can write the electron–hole interaction wavefunction as

$$\chi_{\mathrm{ex}}(\boldsymbol{r}, \boldsymbol{r}') = \sum_{\mathrm{e,h}} A_{\mathrm{e,h}} \psi_{\mathrm{e}}^{\mathrm{QP}}(\boldsymbol{r}) \psi_{\mathrm{e}}^{\mathrm{QP}}(\boldsymbol{r}'). \tag{49}$$

The excitations and expansion coefficients ($A_{\mathrm{e,h}}$) can be obtained from the Bethe–Salpeter (BS) equation:

$$(E_{\mathrm{e}}^{\mathrm{QP}} - E_{\mathrm{h}}^{\mathrm{QP}}) A_{\mathrm{eh}} + \sum_{\mathrm{e}',\mathrm{h}'} K_{\mathrm{e,h,e}',\mathrm{h}'}(\Omega_{\mathrm{ex}}^{\mathrm{BSE}}) A_{\mathrm{e}',\mathrm{h}'} = \Omega_{\mathrm{ex}}^{\mathrm{BSE}} A_{\mathrm{e,h}}. \tag{50}$$

$K$ is an e–h coupling matrix that contains a direct Coulomb interaction and exchange [76]. This formalism works very well for crystalline matter, even for highly ionic materials that possess a large e–h interaction. However, applications to noncrystalline matter are computationally intensive. Supercells are currently used to model the systems of interest. This approach often involves a rather large plane wave basis to replicate 'vacuum'. As such, few calculations for clusters of more than a few dozen atoms exist [76, 77].

Within DFT, we may solve for the *ground state* energy, $E_0$, of a diatomic molecule as a function of the bond length, $R$. We obtain the excitation energy, $E_I$, as a function of $R$ using

$$E_I(R) = E_0(R) + \Omega_I(R). \tag{51}$$

$\Omega_I(R)$ corresponds to the excitation as found in equation (27). LDA is known to give reasonable bond lengths and vibrational frequencies. As such, we expect $E_0(R)$ to represent accurately the ground state energy. In addition, we focus only on singlet excited states, although triplet excited states can be computed through the same approach.

We note that it should be possible to use this expression to find forces for excited states:

$$\frac{\partial E_I(R)}{\partial R} = \frac{\partial E_0(R)}{\partial R} + \frac{\partial \Omega_I(R)}{\partial R}. \tag{52}$$

Finding the derivative of the ground state energy is straightforward. The derivative of the excitation energy is more cumbersome, but it can be evaluated from equations (26) and (27) [78]. This formalism can be used to describe excited relaxations such as those occurring in photochemical reactions. A similar approach has been used in GW–BSE methods [79].

In figures 2 and 3, and table 1, we give results from GW–BSE and TDLDA and compare to experiment. The ground state configuration for BeO and CO is known to be $\mathrm{X}\,^1\Sigma^+$. For BeO, LDA gives a bond length of 1.34 Å; the experimental value is 1.33 Å [80]; the corresponding numbers for CO are 1.25 and 1.24 Å, respectively. In this particular example, GW–BS and TDLDA give comparable results; both agree well with experiment. This is not atypical; TDLDA can be as accurate as GW–BS for small molecules [78].

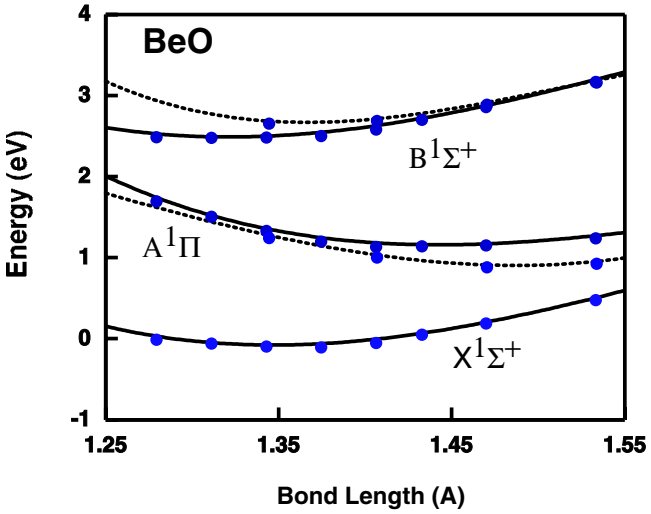


**Figure 2.** Optical excitation energies for a BeO molecule as a function of bond length. For the excited states, the solid curves are for a TDLDA calculation as outlined in the text. The dashed curves are for a GW–BSE solution. The curves represent a cubic fit.

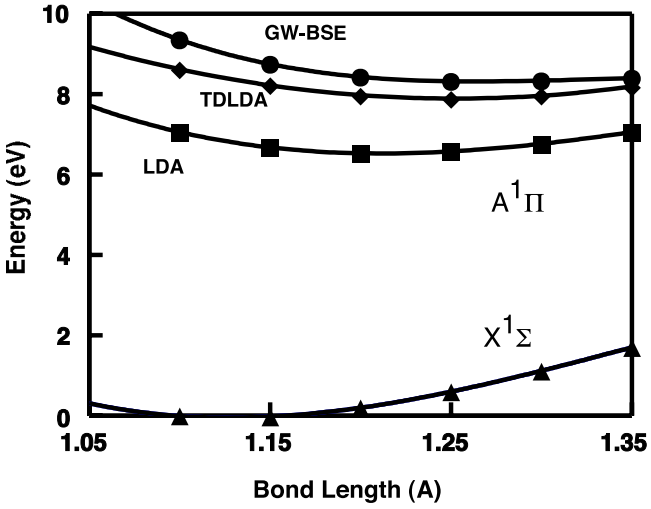


**Figure 3.** Optical excitation energies for a CO molecule as a function of bond length. Show are three calculations: static LDA for the ground state, TDLDA and GW–BSE results for the excited state. See text for details. The curves represent a cubic fit.

### *3.2. Passivated silicon clusters and quantum dots*

The study of hydrogenated silicon clusters and quantum dots is essential for understanding the absorption and emission of visible light in porous silicon [1]. As such, $Si_nH_m$ clusters have been the subject of intensive experimental [81–85] and theoretical [77, 86–91] research. Inconsistencies between the different theoretical models used to describe electronic excitations in these systems remain a subject of contention. For the most part, the inconsistencies arise

**Table 1.** Excited states and bond lengths for BeO and CO molecules.

| Electronic configuration | Energy (eV) | | | Bond length (Å) | | |
|---|---|---|---|---|---|---|
| | TDLDA | GW–BSE | Expt | TDLDA | GW–BSE | Expt |
| A $^1\Pi$ [BeO] | 1.14 | 0.91 | 1.17 | 1.44 | 1.49 | 1.46 |
| B $^1\Sigma^+$ [BeO] | 2.47 | 2.67 | 2.64 | 1.32 | 1.37 | 1.36 |
| A $^1\Pi$ [CO] | 7.9 | 8.3 | 8.1 | 1.25 | 1.25 | 1.24 |

from the formulation of the optical gap in confined systems and the calculation of different components comprising the optical gap [92–95].

The primary focus of theoretical studies is the size dependence of photoluminescence energies and photoabsorption gaps [85, 86, 88, 90–92, 96]. In many cases, such studies do not evaluate oscillator strengths and cannot explicitly identify optically allowed and forbidden transitions [30]. This creates uncertainties in the theoretical interpretation of the experimentally measured optical absorption. The scarcity of theoretical studies dealing with the optical spectra for larger clusters can be explained by the complexity of such calculations, e.g. the difficulty in describing many-body effects in confined systems and the large number of degrees of freedom for these systems.

Structures of $Si_nH_m$ clusters can be obtained by starting with the coordinates of bulk silicon and minimizing the interatomic forces acting on silicon and hydrogen atoms. Atomic forces can be minimized by a variable metric algorithm [97]. This algorithm offers substantial savings in computer time over the standard steepest-descent method. For larger clusters, i.e., clusters with more than $\sim$50 Si atoms, one often relaxes only the outer layers and in particular the Si–H bond length. Structures of selected $Si_nH_m$ clusters are shown in figure 4.

One needs to test boundary conditions used in real-space implementations. For example, one typically requires a 10–12 au separation between the surface atoms at the boundary of the computational domain. Also, in the calculation for TDLDA transition matrix elements, one usually includes two to three times as many unoccupied states as the number of occupied electronic states. These conditions are sufficient to achieve convergence of the computed spectra in the experimentally important optical region below 10 eV.

The calculated absorption spectra of $Si_nH_m$ clusters are shown in figure 5. Only electronic transitions below a given energy threshold are displayed owing to computational constraints. We also show the spectra of time-independent Kohn–Sham LDA eigenvalues. As in the case of metallic and semiconductor clusters with free surfaces [36, 98, 99], the TDLDA spectra of $Si_nH_m$ clusters are blue-shifted with respect to the Kohn–Sham eigenvalue spectra. Unlike optical spectra of 'bare' semiconductor clusters considered in the previous section, the spectra of hydrogenated silicon clusters do not display low-energy transitions associated with the surface states. Photoabsorption gaps for $Si_nH_m$ clusters are much larger than those of $Si_n$ clusters with open surfaces.

In table 2, we compare TDLDA values for the excitation energies of the first three $Si_nH_m$ clusters with experimental data [81, 90] as well as with the values calculated using the BS technique [77]. The last column in table 2 shows the Kohn–Sham LDA 'ionization' energies of the clusters, $-\epsilon^{\mathrm{LDA}}_{\mathrm{HOMO}}$, given by the negative values of the energies for the highest occupied LDA electronic orbitals. Table 2 demonstrates that the calculated TDLDA excitation energies for the transitions below, or close to, $-\epsilon^{\mathrm{LDA}}_{\mathrm{HOMO}}$ agree well with the experimental data and the BS values. The agreement, however, deteriorates for higher excitations, which lie above $-\epsilon^{\mathrm{LDA}}_{\mathrm{HOMO}}$. As the size of clusters increases, the energy of the first allowed excitation moves further down from the LDA 'ionization' energy, and agreement with experiment improves.

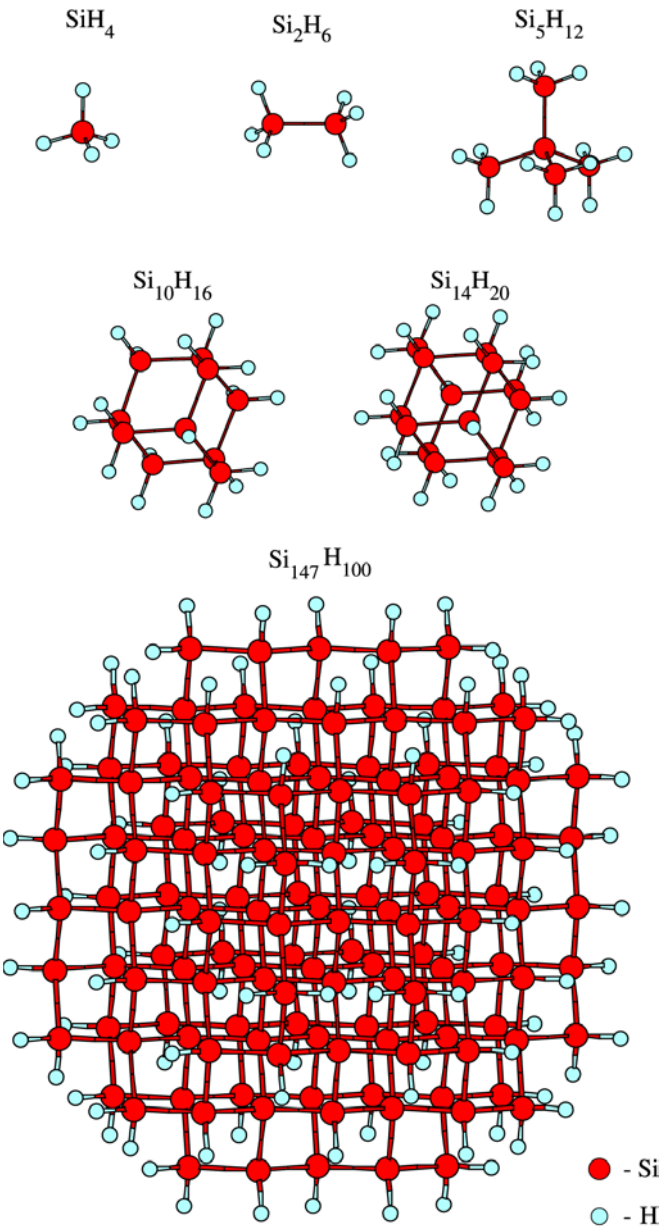


**Figure 4.** Ball and stick models for hydrogenated silicon clusters.

For large $Si_nH_m$ clusters, we found that the first allowed optical transitions are always located below $-\epsilon^{\rm LDA}_{\rm HOMO}$. On this basis, we believe that TDLDA should provide an accurate description for the photoabsorption gaps and the low-energy optical transitions in larger $Si_nH_m$ clusters.

The optical absorption gaps for small clusters can be defined directly by the energy of the first dipole-allowed transition in their absorption spectra. For large clusters, the absorption spectra become essentially quasi-continuous. A large number of low-intensity transitions exist near the absorption edge. Taken individually, the oscillator strengths of these transitions

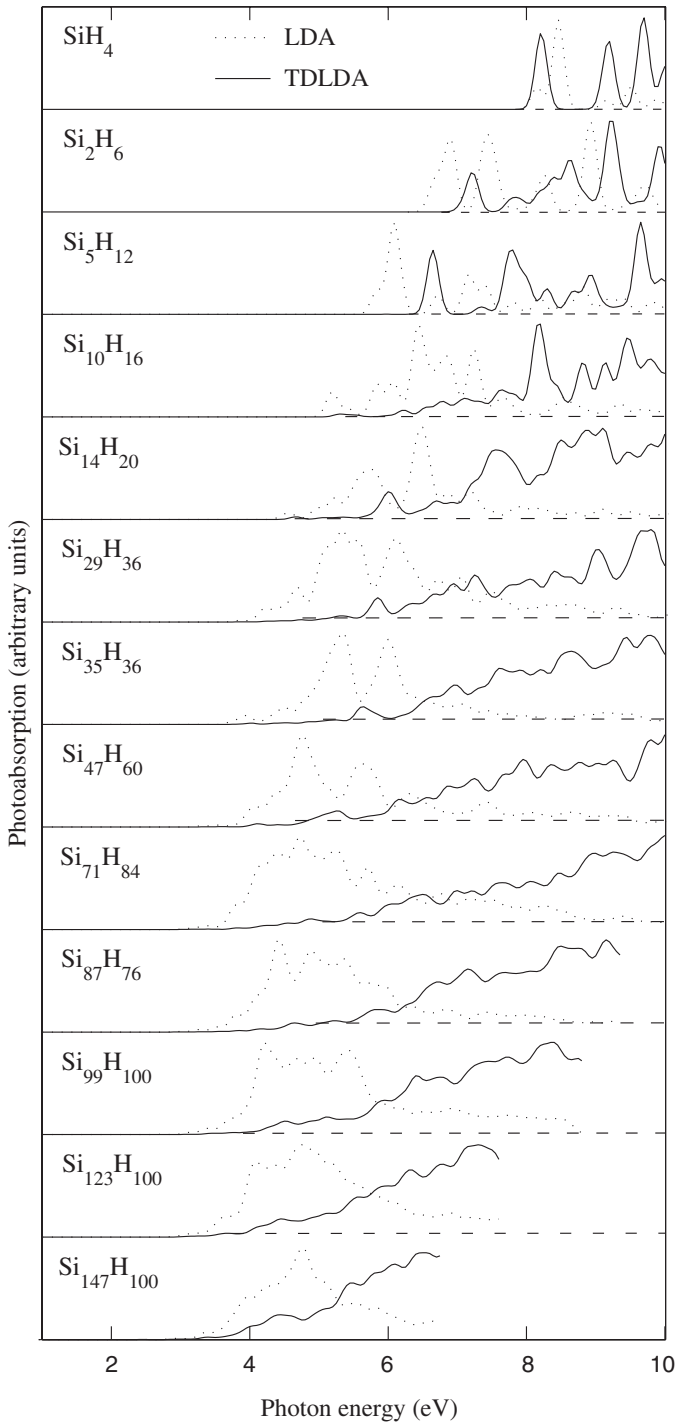


**Figure 5.** Calculated TDLDA absorption spectra of $Si_nH_m$ clusters (solid curves). Spectra of time-independent Kohn–Sham LDA eigenvalues (dotted curves) are shown for comparison. All spectra are broadened by 0.1 eV using a Gaussian convolution. For details see [72].

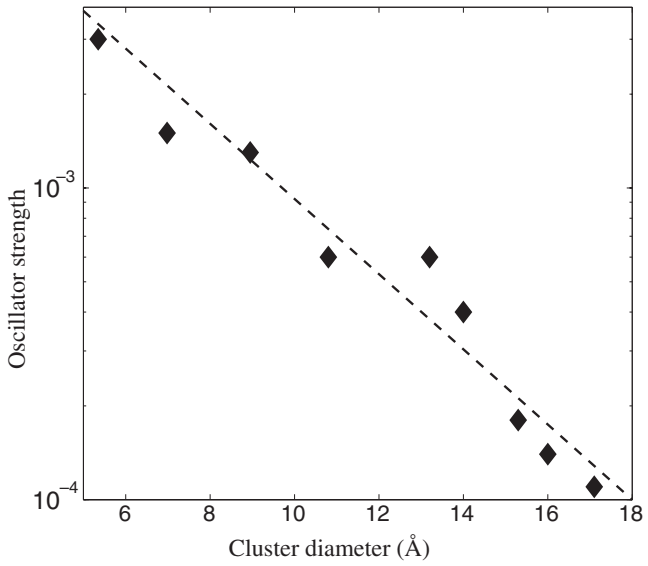


**Figure 6.** Oscillator strength for optical transitions in hydrogenated silicon clusters as a function of cluster size. The strength is determined by considering transitions near the gap. The dashed line is a linear fit.

**Table 2.** Excitation energies of hydrogenated silicon clusters. The experimental optical absorption energies are taken from [81] (silane and disilane) and [90] (neopentasilane). The assignment of electronic excitations for silane and disilane corresponds to the Rydberg transitions. The BS excitation energies are adapted from [77]. $-\epsilon^{\mathrm{LDA}}_{\mathrm{HOMO}}$ is the time-independent LDA 'ionization' energy. All values are in electronvolts.

| Cluster | Transition | Experiment | BS | TDLDA | $-\epsilon^{\mathrm{LDA}}_{\mathrm{HOMO}}$ |
|---|---|---|---|---|---|
| $SiH_4$ | 4s | 8.8 | 9.0 | 8.2 | 8.6 |
| | 4p | 9.7 | 10.2 | 9.2 | |
| | 4d | 10.7 | 11.2 | 9.7 | |
| $Si_2H_6$ | 4s | 7.6 | 7.6 | 7.3 | 7.5 |
| | 4p | 8.4 | 9.0 | 7.8 | |
| $Si_5H_{12}$ | — | 6.5 | 7.2 | 6.6 | 7.3 |

would be located far below the experimentally detectable limit. As a result, identifying the first allowed optical transition in the case of large clusters is not a trivial task. As the size of clusters increases, the absorption gaps gradually decrease, and the discrete spectra for small clusters evolve into quasi-continuous spectra for silicon nanocrystals. Figure 6 demonstrates that oscillator strength of dipole-allowed transitions near the absorption edge decreases with increasing cluster size. This fact is consistent with the formation of an *indirect* bandgap in the limit of bulk silicon [90].

Rather than associating the optical gaps with the individual transitions, one can define a procedure for fixing the optical gap, $E^{\mathrm{opt}}_{\mathrm{gap}}$, via an integral of the oscillator strength. In particular, the following prescription has been suggested [100] to define the gap:

$$pF = \int_0^{E^{\mathrm{opt}}_{\mathrm{gap}}} \sigma(\omega)\,\mathrm{d}\omega \tag{53}$$

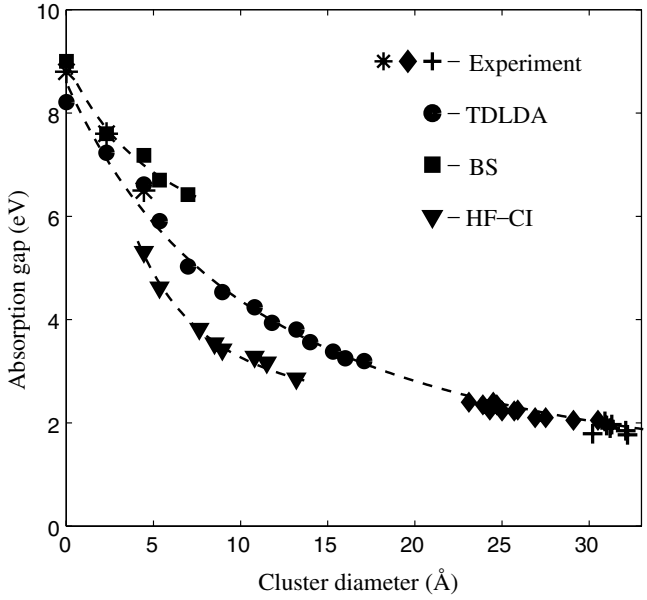


**Figure 7.** Variation of optical absorption gaps as a function of cluster diameter. Theoretical values shown in the plot include the gaps calculated by the TDLDA method (see [72]), by the BS technique [77] and by the Hartree–Fock method with the correlation included through the HF–CI [91]. Experimental values are taken from [81–83, 90]. The dashed curves are a guide to the eye.

where $F$ is the total optical cross section, $\sigma(\omega)$ is the optical cross section for a given frequency, $\omega$, and $p$ is some prescribed fraction of the total cross-section for the fixing the gap. For the photoabsorption gaps, a typical value of $p$ might be $10^{-4}$. This definition for the absorption gap does not affect the values of the optical gaps for small $Si_nH_m$ clusters, since the intensity of their first allowed transitions is much higher than the selected threshold. An order of magnitude change in $p$ does not typically change the gap size by more than 0.1 eV. At the same time, equation (53) offers a convenient method for the evaluation of optical gaps in large clusters.

The variation of the optical absorption gaps as a function of cluster size is shown in figure 7. Along with the TDLDA values, we include optical gaps calculated by the BS technique [77]. For very small clusters, $SiH_4$, $Si_2H_6$, and $Si_5H_{12}$, the gaps computed by the TDLDA method are close to the BS values, although for $Si_{10}H_{16}$ and $Si_{14}H_{20}$ our gaps are considerably smaller than the BS gaps. The TDLDA gaps for clusters in the size range from 5 to 71 silicon atoms are larger by $\sim$1 eV than the gaps calculated by the Hartree–Fock technique with the correlation correction included through the configuration-interaction approximation (HF–CI) [91].

These differences are consistent with the fact that the BS calculations systematically overestimate and the HF–CI calculations of [91] underestimate the experimental absorption gaps. For example, for the optical absorption gap of $Si_5H_{12}$ the BS, TDLDA, and HF–CI methods predict the values of 7.2, 6.6, and 5.3 eV, respectively, compared to the experimental value of 6.5 eV. However, it is not clear whether the gaps of [91] refer to the optically allowed or optically forbidden transitions, which may offer a possible explanation for the observed discrepancy. For large clusters, we find the TDLDA optical gaps to be in generally good agreement with the photoabsorption gaps evaluated by the majority of self-energy corrected LDA [90, 96] and empirical techniques [88, 89, 101]. At present, the full TDLDA calculations

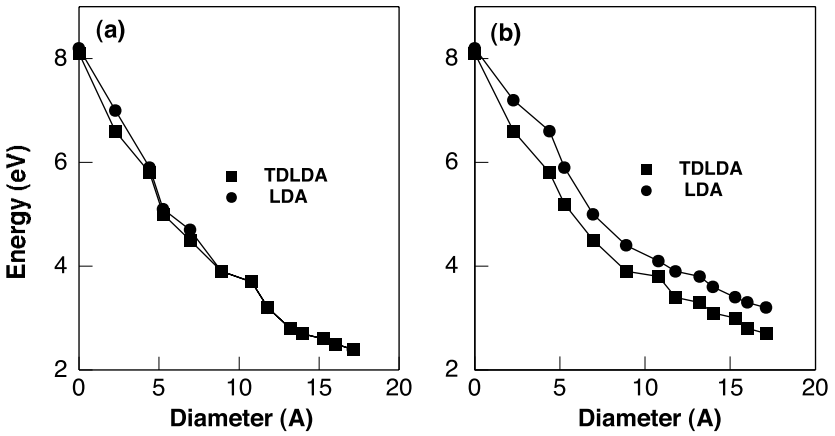


**Figure 8.** Gaps determined from LDA and TDLDA for hydrogenated silicon clusters. (a) The gaps plotted without regard to the oscillator strength. (b) The gaps determined using the criteria from equation (53).

for clusters larger than a few nanometres can exceed the capabilities of most computational platforms. Nevertheless, the extrapolation of the TDLDA curve in the limit of large clusters comes very close to the experimental values for the photoabsorption gaps. Software and hardware advances should make a direct verification of this possible in the near future.

### *3.3. The role of oscillator strengths in fixing the optical gap*

In determining the optical gaps within a linear response approach, only excitations with an induced dipole are incorporated. In real-time methods, the induced dipole term is calculated directly [40–42]. Within our frequency domain description, two factors enter into ascertaining the existence of an induced dipole: the existence of a transition energy and the corresponding oscillator strength. Within TDLDA, these terms can be obtained from equation (27) as $\Omega_I$ and $\boldsymbol{F}_I$. These terms must always be considered together when predicting optical properties, although sometimes this is not done [30].

In figure 8, we illustrate the lowest transitions without regard to oscillator strength for both LDA and TDLDA calculations. We also illustrate transitions as defined by equation (53). For these transitions, the gap is defined when the oscillator strength assumes a value of at least $10^{-4}$ of the total optical cross-section. The main difference between LDA and TDLDA for these systems is a strong blue-shift of the oscillator strength. This effect can also be documented for smaller hydrogenated silicon molecules. In figure 9, we illustrate the optical spectrum using LDA and weighting each transition by the dipole matrix element. We do the same for the TDLDA spectrum. The threshold for the LDA transition is approximately 5.8 eV, which is the same as the lowest TDLDA eigenvalue, $\Omega_0$, as determined from equation (27), to within 0.1 eV. However, the spectrum clearly indicates that significant optical absorption does not occur until nearly 6.6 eV. This value is consistent with experiment. For the majority of the hydrogenated clusters, with $SiH_4$ being an exception, the oscillator strength of the first TDLDA transition vanishes. The difference between the lowest transition and the first allowed optical transition can be significant. This suggests that TDLDA methods based on a single-pole approximation [24, 25] without regard to the oscillator strength will not successfully describe these systems.

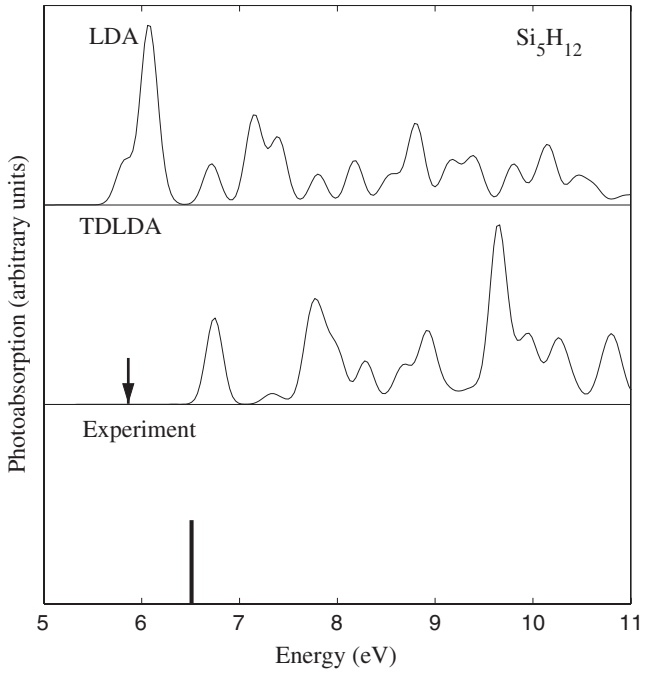


**Figure 9.** Calculated optical spectra for $Si_5H_{12}$ using LDA and TDLDA. The arrow in the TDLDA panel shows the lowest eigenvalue from equation (27). The experiment shows the measured optical gap as quoted in [90].

It should be noted that real-time methods for TDLDA do not require an knowledge of unoccupied eigenvalues [40–42]. In this formalism, the absorption spectrum evolves from taking the power spectrum of the instantaneous induced dipole. The resolution of an optical transition is determined by the length of the time integration [40–42].

### *3.4. The role of oxygen in silicon quantum dots*

Porous and nanocrystalline silicon studied in experiments are prepared under a variety of surface conditions determined by the etching technique and external chemical environments employed. Only a fraction of published experimental data refers to 'pure' hydrogenated silicon dots [82]. Other measurements are performed on partially oxidized nanocrystals [102, 103]. For many cases, a precise chemical composition of nanocrystalline surfaces is not known [83, 104, 105].

However, most calculations for optical absorption and emission in silicon dots do not take into account differences in structure and chemical composition of the dot surface. This creates an ambiguity in the interpretation of experimental data. Almost all *ab initio* and empirical simulations available in the literature use silicon dots passivated with hydrogen [77, 86, 89–91, 96, 101, 106], although some notable exceptions exist [107, 108]. This limitation is also true for structural issues, where only a few systems have been examined for reconstructed surfaces [109, 110].

Theoretical calculations [77, 86, 89–91, 96, 101, 106] based on a quantum confinement model show general agreement with experimental measurements [82] for optical absorption in hydrogen-passivated silicon clusters. In contrast, experiments performed on oxidized samples often display photoluminescence with energies significantly below the values of

optical gaps predicted by the confinement model for clusters in the same size range [102, 103]. This disagreement could be greater than 1 eV. It has been suggested that the onset of photoluminescence in silicon nanocrystals may be associated with the optical Stokes shift [111] and excitonic exchange splitting [112]. While these effects could be significant in small silicon dots, it appears that neither the Stokes shift, nor the excitonic exchange splitting alone, could explain such a large disagreement between experiment and theory.

Recent experimental data present strong evidence that surface effects produce a very substantial impact on the electronic and optical properties of nanocrystalline silicon. Specifically, Wolkin *et al* [84] observed a large red-shift of photoluminescence in porous silicon after exposure to air. The study reported a shift of photoluminescence of the order of 1 eV for samples composed of crystallites smaller than 2 nm in size. The observed red-shift has been attributed to surface oxidation of silicon nanocrystals. According to the interpretation proposed in [84], oxygen creates trapped electron and hole states on nanocrystalline surfaces. The trapped surface states reduce the effective size of the optical gap. This mechanism can explain the difference between the energy of the measured photoluminescence and theoretical predictions based on the quantum confinement model.

Owing to a very large number of possible configurations for oxidized silicon clusters, current studies are often limited to the case of a single oxygen atom attached to the cluster surface. Oxidized clusters were prepared from regular hydrogen-terminated spherical dots by replacing two hydrogen atoms on the surface with a single atom of oxygen, followed by relaxation of all interatomic forces. The model geometries for oxidized clusters are illustrated in figure 10.

The calculated absorption spectra of oxidized silicon dots are shown in figures 11 and 12. In figure 11 the spectra of small oxidized and unoxidized clusters are illustrated. The addition of oxygen creates new absorption bands in the region of lower transition energies. Optical excitations with higher energies are also affected by oxidation, although some intense absorption peaks observed in unoxidized clusters (such as the peaks at 6.6 and 7.8 eV for $Si_5H_{12}$) appear to be only slightly shifted. Figure 12 shows the calculated spectra of the $Si_{29}OH_{34}$ and $Si_{35}OH_{34}$ clusters.

The change in the optical absorption spectrum caused by the addition of a single oxygen atom is small in larger clusters. To make the effect of oxidation more evident, we plot in figure 12 the differential spectra calculated as the difference in optical absorption of the same cluster before and after oxidation. Positive values of differential photoabsorption correspond to the new absorption peaks that appear only after oxidation. The differential absorption spectra for $Si_{29}OH_{34}$ and $Si_{15}OH_{34}$ clearly show the presence of low-energy optical transitions associated with surface oxygen. The calculated optical absorption gaps in oxidized and unoxidized silicon dots are compared in figure 13. The TDLDA gaps for unoxidized $Si_nH_m$ clusters are adapted from our previous work [106]. The spectra are essentially quasicontinuous and exhibit a large number of low-intensity transitions near the absorption edge. As such, the effective optical gaps were evaluated at a very small but nonzero fraction of the complete electronic oscillator strength as in equation (53). The same criterion in defining the gap for silicon quantum dots was used for the oxidized silicon clusters. Figure 13 demonstrates that surface oxidation reduces optical gaps in hydrogenated silicon clusters by as much as 1–2 eV. The change in the size of optical gaps is consistent with the red-shift of photoluminescence observed in [84] and is probably responsible for the disagreement between experimental photoluminescence from oxidized silicon nanocrystals and theoretical estimates based on the quantum confinement model.

A surprising result of oxygen absorption is the small difference observed in the optical gaps between cluster isomers with Si=O and Si–O–Si bonds on the surface. At the same time,

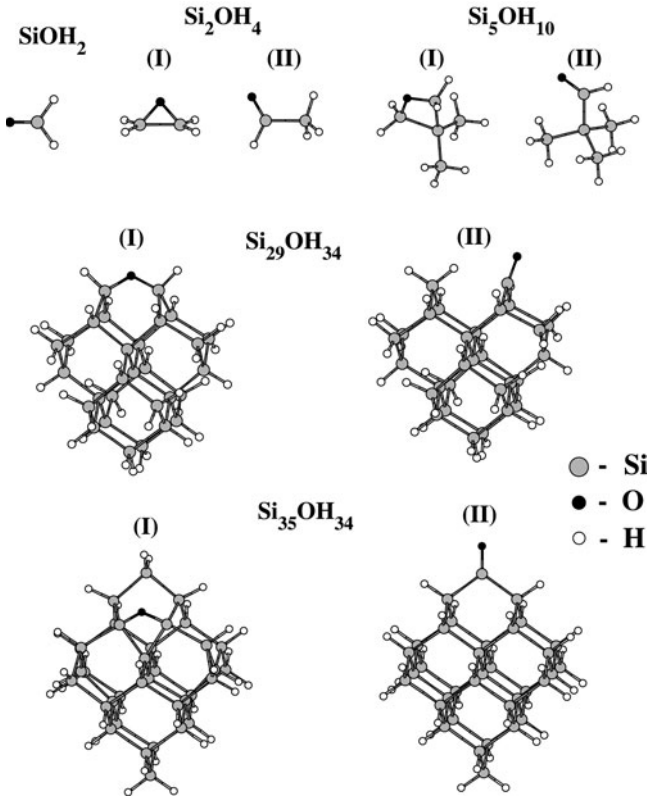


**Figure 10.** Model geometries for hydrogenated silicon with oxygen.

figures 11 and 12 reveal substantial differences in the shapes of optical spectra for these clusters. One can understand this difference by examining the mechanism of the gap formation in two selected clusters: $Si_{35}OH_{34}$ (I) and (II). The order of electronic levels near the gap is illustrated for both isomers in figures 14 and 15, respectively. These diagrams represent simplified schemes that show only the dominant single-electron Kohn–Sham transitions within the TDLDA description and do not account for correlations among individual excitations. The energies of optical transitions shown in these figures correspond to one-electron singlet TDLDA excitations [36]. They differ from transition energies of the TDLDA optical spectra shown in figures 11 and 12, which correspond to collective electronic excitations. Nevertheless, the single-electron diagrams are useful for the qualitative analysis of optical transitions in oxidized silicon dots. The authors of [84] proposed that photoluminescence in small oxidized silicon clusters occurs between the trapped electron and hole states, both of which are associated with the double Si=O bond on the cluster surface. Specifically, the trapped electron state is a p state localized on silicon and the trapped hole state is a p state localized on oxygen. Spatial distributions of electron densities for the lowest unoccupied molecular orbital (LUMO) and the highest occupied molecular orbital (HOMO) of the $Si_{35}OH_{34}$ (II) cluster plotted in figure 14 confirm that these states are indeed represented by p states mainly localized on the silicon and oxygen atoms. However, the distributions of HOMO and LUMO electron densities for the $Si_{35}OH_{34}$ (I) cluster shown in figure 15 reveal a different picture. The LUMO state is, for the most part, localized on two silicon atoms that form the Si–O–Si bonds. At the same time,

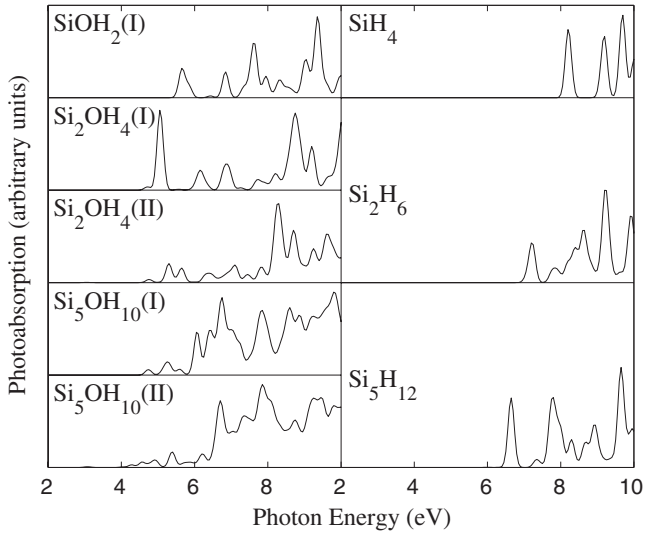


**Figure 11.** Left: calculated TDLDA absorption spectra of oxidized hydrogen-terminated silicon clusters [110]. Right: TDLDA spectra of unoxidized clusters. All spectra were broadened by 0.1 eV using a Gaussian convolution.

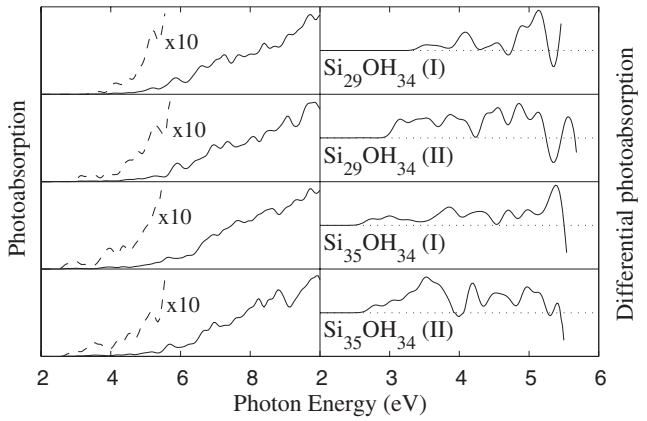


**Figure 12.** Left: calculated TDLDA absorption spectra of $Si_{29}OH_{34}$ and $Si_{35}OH_{34}$ clusters [110]. Right: difference in optical absorption between clusters with and without oxygen on the surface. All spectra are broadened by 0.1 eV.

the HOMO state is not localized on the oxygen atom. Instead, this electronic state is spread among the layers of silicon atoms surrounding the Si–O–Si fragment. In both cases, the direct dipole transitions between the HOMO and LUMO states are forbidden. The absorption edge for $Si_{35}OH_{34}$ (II) is formed mainly by transitions from lower occupied orbitals to the LUMO state. For this cluster, transitions from the HOMO state to higher unoccupied orbitals do not contribute to optical absorption near the gap. For $Si_{35}OH_{34}$ (I), however, both of these types of electronic transition are involved in the formation of the absorption edge.

Such calculations show that even a low concentration of oxygen on the surface can substantially alter the optical properties of silicon nanoclusters. However, experimental studies are not always limited to clusters with low oxygen content. Some limited studies have been

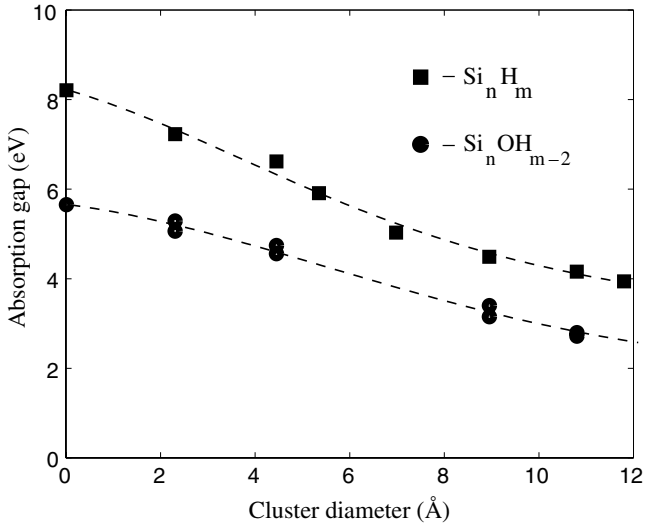


**Figure 13.** Comparison between the optical absorption gaps of regular and oxidized hydrogen-terminated silicon clusters. The gaps for SiH clusters are adapted from [106]. The dashed curves are a guide to the eye.

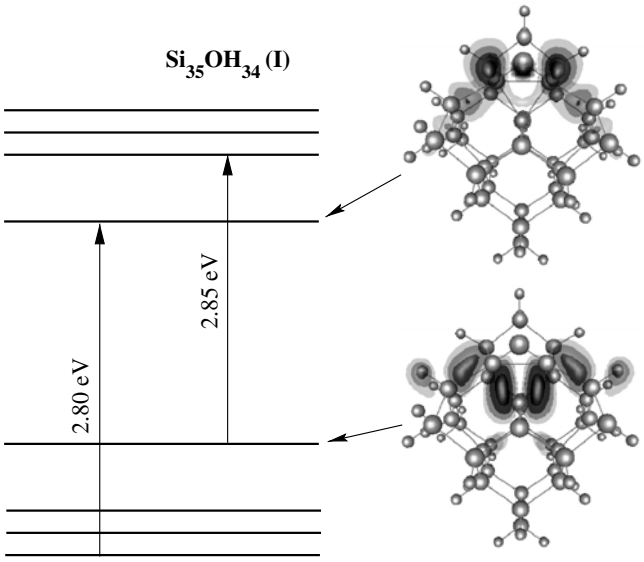


**Figure 14.** Schematic representation of electronic levels in the vicinity of the gap for $Si_{35}OH_{34}$ (I) clusters [110]. Spatial distributions of electron densities are shown for the HOMO and LUMO states.

performed on dots with a higher concentration of oxygen, e.g., $Si_{35}O_6H_{24}$. This cluster was prepared from the hydrogen-terminated dot $Si_{35}H_{36}$ by replacing 12 outer-shell hydrogen atoms with oxygen to form six double Si=O bonds at the positions symmetrically equivalent to that shown in figure 10 for $Si_{35}OH_{34}$ (II). The increase in oxygen coverage caused a further reduction of the absorption gap to 2.4 eV. This value was approximately 0.4 eV lower than

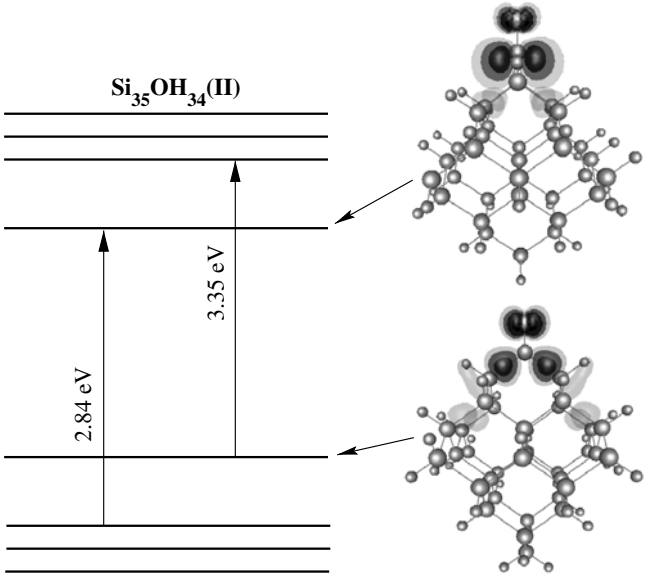


**Figure 15.** Schematic representation of electronic levels in the vicinity of the gap for $Si_{35}OH_{34}$ (II) clusters [110]. Spatial distributions of electron densities are shown for the HOMO and LUMO states.

the absorption gap for $Si_{35}OH_{34}$ (II), and almost 1.6 eV lower than the gap for the unoxidized cluster $Si_{35}H_{36}$. The principal mechanism of gap formation for $Si_{35}O_6H_{24}$ appears to be similar to that for $Si_{35}OH_{34}$. The additional reduction of the absorption gap in the case of $Si_{35}O_6H_{24}$ could be explained by interactions among oxygen-induced electronic states. The absorption gap for $Si_{35}OH_{34}$ is reduced by the presence of localized oxygen-induced levels. In the limit of large clusters, the positions of these levels should be essentially independent of the cluster size. Since the gaps in silicon dots decrease with increasing cluster size as a result of diminishing quantum confinement, at some point the oxygen-induced states are expected to cross over the electronic levels from the body of the cluster. After this point, the oxygen-induced states would no longer be located inside the gap. Calculations suggest that, depending on the fraction of oxygen coverage, the oxygen-induced states should not cross over the levels from the body of the cluster for silicon dots up to approximately 20–25 Å in diameter [107]. For larger dots, the overall effect of surface oxidation on the optical properties is likely to be less important.

### *3.5. CdSe quantum dots*

While silicon is the premier electronic material, it is problematic as to whether it is the material of choice for quantum dots [113]. In particular, much work has been devoted to the study of the optical onset in colloidally prepared II–VI semiconductors [114–116].

The size of such quantum dots can be used to tune the optical gap across a major portion of the visible spectrum. For example, in the case of CdSe, the optical gap can be tuned from the deep red (1.7 eV) to green (2.4 eV) by reducing the dot diameter from 20 to 2 nm [114, 115]. The ability to use 'size' as a variable in tailoring the desired properties of the system has made II–VI quantum dots promising materials for the development of new electronic and optical devices such as light emitting diodes [114] and solar cells [117].

One way of synthesizing II–VI quantum dots is allowing molecular or ionic precursors to react together in solution forming the dots as colloids. CdSe and CdS have been two of the most studied II–VI dots due to the availability of precursors, the ease of their crystallization, and the fact that their optical gap can be in the visible range. CdX (X = S, Se) quantum dots can be synthesized by mixing $Cd(CH_3)_2$ with a chalcogenide reagent in a coordinating solvent. A solvent commonly used is a mixture of TOP and TOPO (trioctyl phosphine and trioctyl phosphine oxide), which acts as a surfactant [115]. This method leads to highly monodisperse quantum dots passivated with TOP/TOPO. These quantum dots can also be terminated with other capping agents such as thiolates, pyridine, or selenophenols [118–120].

Several empirical and semiempirical theoretical studies of CdX quantum dots have been reported [121, 122]. Wang and Zunger [121], and later Rabani *et al* [122], calculated optical gaps of CdSe quantum dots using an empirical pseudopotential method. The results obtained by these authors compare well with experiment. In their work, they used a ligand potential model [121] in order to simulate the surface passivation. This model places a short-range electrostatic potential near the surface atoms. The potentials are taken to be Gaussians that are placed in the direction of the missing atom. However, the choice of the magnitude of the potential and the width of the Gaussian, as well as the distance from the centre of the Gaussian to the surface atom, can change the values of the calculated optical gaps.

It is possible to examine such systems using TDLDA as implemented for silicon quantum dots. However, the pseudopotentials for II–VI semiconductors must be carefully crafted. The outlying cation d states cannot be considered as true core states as the core–valence charge overlap is significant [99]. In the case of the Cd pseudopotential, one option is to include the 4d states as part of the valence shell. This procedure would necessitate using a finer grid in real space and more than doubling the required number of valence electrons. This option is viable, although it greatly increases the computational load [99]. Another option is to include the effect of the 4d implicitly via a 'core correction' [51] as outlined in section 2.1 (equation (7)).

A few studies using TDLDA or related methods have been applied to CdSe quantum dots. One is by Deglmann *et al* [123]. In this work, they calculated the optical gaps for CdSe quantum dots using a time-dependent density functional formalism. The structures of the CdSe quantum dots were optimized with symmetry restrictions. The final structures of the quantum dots calculated using this method do not have the bulk structure. In fact, the resulting structures are strongly distorted from that of the bulk crystal, and the bond lengths are significantly larger. This is in disagreement with experimental findings [115]. Their calculated optical gaps differ from those obtained experimentally. For most of the dots they studied, the value of the optical gap is already smaller than that of the bulk phase, even for the smaller dots. Another study has been performed by Eichkorn and Ahlrichs [124]. In this work, quantum dots were modelled using a ligand-stabilized cluster of CdSe. A few low-lying excitations were determined using TDLDA. However, the dots examined were not stoichiometric.

Real-space pseudopotential calculations have been performed using TDLDA for the optical absorption spectra and optical gaps of $Cd_nSe_n$ quantum dots ($n = 17, 26$ and 38) [125]. The dots studied are spherical fragments of the wurtzite crystal. Owing to the large number of atoms of the capping agents and uncertainty in the local geometry of the TOPO/TOP–quantum dot interface, it is not feasible to model this system directly. In these studies, the surface atoms were fixed to replicate the bulk geometry and the surface atoms were not capped with any passivating agent [125]. This procedure has a number of advantages. From a computational point of view, it is not necessary to extract eigenvalues of species that are expected to be electronically inert. Moreover, it removes uncertainties associated with variant capping species. Figure 16 shows the structures of the quantum dots correspond to clusters of $Cd_{17}Se_{17}$, $Cd_{26}Se_{26}$, and $Cd_{38}Se_{38}$, respectively.

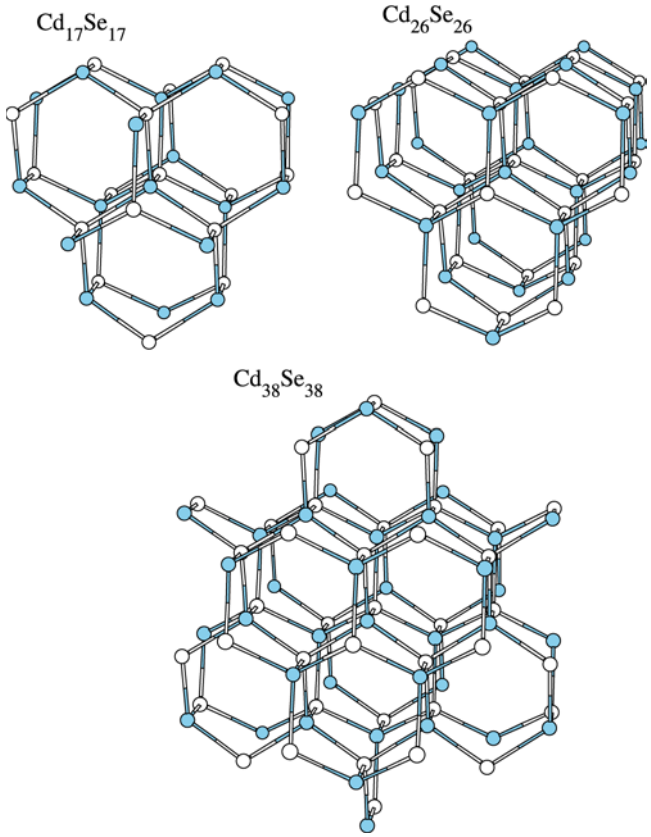


**Figure 16.** Structures of $Cd_{17}Se_{17}$, $Cd_{26}Se_{26}$, and $Cd_{38}Se_{38}$ wurtzite dots.

As noted in the case of hydrogenated silicon dots, it is not straightforward to define an optical gap when the system possess a number of low-lying electronic excitations. This is also the case for unpassivated CdSe quantum dots. This is a disadvantage in using a bare cluster to model a quantum dot; i.e., the dangling bond states have not been explicitly removed by a passivating agent. However, one can construct a well defined procedure to extract a gap as in equation (53).

Figure 17 shows the size dependence of the optical gaps for CdSe quantum dots from theory and experiment. The measured optical gap for the smallest dot shown is 3.8 eV. For sufficiently large dots, one expects the optical gap to converge to the bulk value of 1.7 eV [126]. This is consistent from experimental studies of dots over a wide range of sizes [115, 127]. Figure 3 also shows the optical gaps obtained experimentally by Soloviev *et al* [127], Murray *et al* [115] and Rogach *et al* [128].

It can be observed that the optical gaps calculated using *time-independent* LDA significantly underestimate the experimental gaps as well as the gaps calculated using TDLDA when the '2% rule' is invoked, i.e., a value of $p = 0.02$ is used in equation (53) (as suggested in [100] for small semiconductor clusters of GaAs). Specifically, the LDA gaps are more than 2 eV smaller than the TDLDA values and in poor agreement with experiment. In contrast, the optical gaps calculated using TDLDA show good agreement with the experimental findings, especially with those of Soloviev *et al* [127].

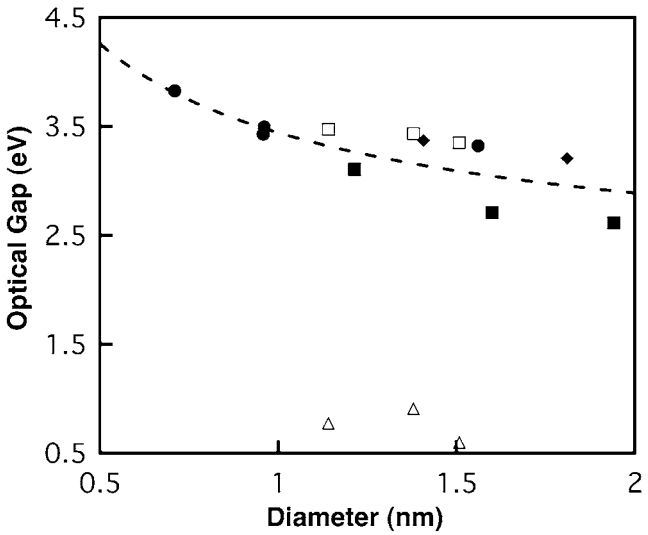


**Figure 17.** Size dependence of the optical gap for CdSe quantum dots. The dashed curve is a guide to the eye, roughly fitted to the measured gaps. Open symbols represent gaps calculated from TDLDA (squares) and LDA (triangles). The solid symbols are measured gaps from Soloviev *et al* [127] (squares), Rogach *et al* [128] (dots), and Murray *et al* [115] (diamonds).

## 4. Conclusions

We have illustrated a method for calculating the optical properties of localized systems including molecules, clusters, and quantum dots. Our method utilizes a real-space description of the electronic structure problem described by pseudopotentials and DFT. The optical properties of these systems can be predicted by using time-dependent DFT and, in particular, the TDLDA. The only additional approximation beyond those in the static electronic structure problem is the *adiabatic approximation*. This approach to optical properties is easy to implement and allows one to consider large systems in a straightforward manner.

In contrast to other methods such as the GW–BS method [76, 77], TDLDA offers an efficient procedure for large systems. When implemented in real space using linear response theory, TDLDA can be applied to systems with several hundred, if not thousands of electrons. At the same time, as a fully *ab initio* technique, TDLDA avoids many of the controversies associated with empirical or semi-empirical methods. The *ab initio* nature of the TDLDA formalism makes it flexible in application to a variety of systems composed of different chemical elements. Moreover, unlike recent advances in quantum Monte Carlo methods [30], TDLDA can yield the full optical spectrum.

## Acknowledgments

We acknowledge helpful discussions with S G Louie and S Ismail Beigi. We would like to acknowledge support from the National Science Foundation and the United States Department of Energy. Computational support was provided by the National Energy Research Scientific Computing Center and the Minnesota Supercomputing Institute. This work was supported in part by the Army High Performance Computing Research Center (AHPCRC) under the auspices of the Department of Army, Army Research Laboratory (ARL) under Cooperative

Agreement number DAAD19-01-2-0014. The content does not necessarily reflect the position or the policy of the government; no official endorsement should be inferred. One of us (LK) acknowledges support of the Estelle Funk Foundation and the Delta Career Development Chair.

## References

[1] Canham L T 1990 *Appl. Phys. Lett.* **57** 1046
[2] Lockwood D J 1994 *Solid State Commun.* **92** 101
[3] Cohen M L and Chelikowsky J R 1989 *Electronic Structure and Optical Properties of Semiconductors* 2nd edn (Berlin: Springer)
[4] Hohenberg P and Kohn W 1964 *Phys. Rev.* B **136** 864
[5] Kohn W and Sham L J 1965 *Phys. Rev.* A **140** 1133
[6] Kohn W and Vashishta P 1983 *Theory of the Inhomogeneous Electron Gas* ed S Lundqvist and N H March (New York: Plenum)
[7] Chelikowsky J R and Cohen M L 1992 *Handbook of Semiconductors* 2nd edn, ed T S Moss and P T Landsberg (Amsterdam: Elsevier)
[8] Payne M C, Teter M P, Allan D C, Arias T A and Joannopoulos J D 1992 *Rev. Mod. Phys.* **64** 1045
[9] Pickett W 1989 *Comput. Phys. Rep.* **9** 115
[10] Srivastava G P and Weaire D 1987 *Adv. Phys.* **36** 463
[11] Beck T L 2000 *Rev. Mod. Phys.* **74** 1041
[12] Chelikowsky J R, Troullier N and Saad Y 1994 *Phys. Rev. Lett.* **72** 1240
[13] Chelikowsky J R, Troullier N, Wu K and Saad Y 1994 *Phys. Rev.* B **50** 11135
[14] Briggs E L, Sullivan D J and Bernholc J 1995 *Phys. Rev.* B **52** R5471
[15] Gygi F and Galli G 1995 *Phys. Rev.* B **52** R2229
[16] Zumbach G, Modine N A and Kaxiras E 1996 *Solid State Commun.* **99** 57
[17] Fattebert J-L and Bernholc J 2000 *Phys. Rev.* B **62** 1713
[18] Pask J E, Klein B M, Sterne P A and Fong C Y 2001 *Comput. Phys. Commun.* **135** 1
[19] Chelikowsky J R, Kronik L, Vasiliev I, Jain M and Saad Y 2003 *Handbook of Numerical Analysis, vol X: Computational Chemistry* (Amsterdam: Elsevier) chapter (Using Real Space Pseudopotentials for the Electronic Structure Problem) p 613
[20] Calvayrac F, Reinhard P-G, Suraud E and Ullrich C 2000 *Phys. Rep.* **337** 493
[21] Fornberg B and Sloan D M 1994 *Acta Numer.* **94** 203
[22] Smith G 1978 *Numerical Solutions of Partial Differential Equation: Finite Difference Methods* 2nd edn (New York: Oxford)
[23] Andreoni W 1990 *The Chemical Physics of Atomic and Molecular Clusters* ed G Scoles (Amsterdam: North-Holland) p 159
[24] Gross E K U, Dobson J F and Petersilka M 1996 *Density Functional Theory* ed R F Nalewajski (Berlin: Springer) p 81
[25] Petersilka M, Gossmann U J and Gross E K U 1996 *Phys. Rev. Lett.* **76** 1212
[26] Saunders V R and van Lenthe J H 1983 *Mol. Phys.* **48** 923
[27] Buenker R J, Peyerimhoff S D and Butscher W 1978 *Mol. Phys.* **35** 771
[28] Bernu B, Ceperley D M and Lester W A Jr 1990 *J. Chem. Phys.* **93** 552
[29] Bernu B, Ceperley D M and Lester W A Jr 1991 *J. Chem. Phys.* **95** 7782
[30] Williamson A J, Grossman J C, Hood R Q, Puzder A and Galli G 2002 *Phys. Rev. Lett.* **89** 196803
[31] Sham L J and Rice T M 1966 *Phys. Rev.* **144** 708
[32] Hedin L 1965 *Phys. Rev.* A **139** 796
[33] Hybertsen M S and Louie S G 1986 *Phys. Rev.* B **34** 5390
[34] Casida M 1995 *Recent Advances in Density-Functional Methods* part I, ed D Chong (Singapore: World Scientific) p 155
[35] Casida M 1996 *Recent Developments and Applications of Modern Density Functional Theory* ed J Seminario (Amsterdam: Elsevier) p 391
[36] Vasiliev I, Öğüt S and Chelikowsky J R 1999 *Phys. Rev. Lett.* **82** 1919
[37] Raghavachari K, Ricci D and Pacchioni G 2002 *J. Chem. Phys.* **116** 825
[38] Jaramillo J and Scuseria G E 2000 *Theor. Chem. Acc.* **105** 62
[39] Hirata S and Head-Gordon M 1999 *Chem. Phys. Lett.* **314** 291
[40] Yabana K and Bertsch G F 1996 *Phys. Rev.* B **54** 4484
[41] Yabana K and Bertsch G F 1997 *Z. Phys.* D **42** 219

[42] Yabana K and Bertsch G F 1999 *Int. J. Quantum Chem.* **75** 55
[43] Appel H, Gross E K U and Burke K 2003 *Phys. Rev. Lett.* **90** 043005
[44] Burdick W R, Saad Y, Kronik L, Jain I V M and Chelikowsky J R 2003 *Comput. Phys. Commun.* at press
[45] Onida G, Reining L and Rubio A 2002 *Rev. Mod. Phys.* **74** 601
[46] Kleinman L and Bylander D M 1982 *Phys. Rev. Lett.* **48** 1425
[47] Troullier N and Martins J L 1991 *Phys. Rev.* B **43** 1993
[48] Ceperley D M 1978 *Phys. Rev.* B **18** 3126
[49] Ceperley D M and Alder B J 1980 *Phys. Rev. Lett.* **45** 566
[50] Perdew J P and Zunger A 1981 *Phys. Rev.* B **23** 5048
[51] Louie S G, Froyen S and Cohen M L 1982 *Phys. Rev.* B **26** 1738
[52] Stathopoulos A, Öğüt S, Saad Y, Chelikowsky J R and Kim H 2000 *Comput. Sci. Eng.* **2** 19
[53] Morgan R B and Scott D S 1986 *SIAM J. Sci. Comput.* **7** 817
[54] Deb B M and Ghosh S K 1982 *J. Chem. Phys.* **77** 342
[55] Ghosh S K and Deb B M 1982 *Chem. Phys.* **71** 295
[56] Bartolotti L J 1981 *Phys. Rev.* A **24** 1661
[57] Bartolotti L J 1982 *Phys. Rev.* A **26** 2243
[58] Runge E and Gross E K U 1984 *Phys. Rev. Lett.* **52** 997
[59] Gross E K U and Kohn W 1985 *Phys. Rev. Lett.* **55** 2850
[60] Gross E K U and Kohn W 1990 *Adv. Quantum Chem.* **21** 255
[61] Kootsra F, de Boeji P L and Snijders J G 2000 *Phys. Rev.* B **62** 7071
[62] Velde G T *et al* 2001 *J. Comput. Chem.* **22** 931
[63] Reining L, Olevano V, Rubio A and Onida G 2002 *Phys. Rev. Lett.* **88** 066404
[64] Kim Y H and Görling A 2002 *Phys. Rev. Lett.* **89** 096402
[65] Perdew J P, Burke K and Wang Y 1996 *Phys. Rev.* B **54** 16533
[66] Becke A D 1993 *J. Chem. Phys.* **98** 5648
[67] Casida M E and Salahub D R 2000 *J. Chem. Phys.* **113** 8918
[68] van Leeuwen R and Baerends E J 1994 *Phys. Rev.* A **49** 2421
[69] Vasiliev I 2003 *Phys. Status Solidi* at press
[70] Mahan G D 1981 *Many-Particle Physics* (New York: Plenum)
[71] Beck D E 1991 *Phys. Rev.* B **43** 7301
[72] Vasiliev I, Öğüt S and Chelikowsky J R 2002 *Phys. Rev.* B **65** 115416
[73] Godby R W, Schlüter M and Sham L J 1987 *Phys. Rev.* B **35** 4170
[74] Blase X, Rubio A, Louie S G and Cohen M L 1995 *Phys. Rev.* B **52** R2225
[75] Rojas H N, Godby R W and Needs R J 1995 *Phys. Rev. Lett.* **74** 1827
[76] Rohlfing M and Louie S 2000 *Phys. Rev.* B **62** 4927
[77] Rohlfing M and Louie S G 1998 *Phys. Rev. Lett.* **80** 3320
[78] Kronik L, Ismail-Beigi S, Louie S G and Chelikowsky J R 2003 submitted
[79] Ismail-Beigi S and Louie S G 2003 *Phys. Rev. Lett.* **90** 076401
[80] Radzig A A and Smirnov B M 1985 *Reference Data on Atoms, Molecules and Ions* (Berlin: Springer) p 332
[81] Itoh U, Toyoshima Y, Onuki H, Washida N and Ibuki T 1986 *J. Chem. Phys.* **85** 4867
[82] Furukawa S and Miyasato T 1988 *Phys. Rev.* B **38** 5726
[83] Lockwood D J, Wang A and Bryskiewicz B 1994 *Solid State Commun.* **89** 587
[84] Wolkin M V, Jorne J, Fauchet P M, Allan G and Delerue C 1999 *Phys. Rev. Lett.* **82** 197
[85] Takagahara T and Takeda K 1992 *Phys. Rev.* B **46** 15578
[86] Hill N A and Whaley K B 1995 *Phys. Rev. Lett.* **75** 1130
[87] Delerue C, Lannoo M and Allan G 1996 *Phys. Rev. Lett.* **76** 3038
[88] Delerue C, Allan G and Lannoo M 1993 *Phys. Rev.* B **48** 11024
[89] Wang L W and Zunger A 1994 *J. Phys. Chem.* **100** 2394
[90] Delley B and Steigmeier E F 1993 *Phys. Rev.* B **47** 1397
[91] Baierle R J, Caldas M J, Molinari E and Ossicini S 1997 *Solid State Commun.* **102** 545
[92] Franceschetti A, Wang L W and Zunger A 1999 *Phys. Rev. Lett.* **83** 1269
[93] Öğüt S, Chelikowsky J R and Louie S G 1999 *Phys. Rev. Lett.* **1999** 1270
[94] Godby R W and White I D 1998 *Phys. Rev. Lett.* **80** 3161
[95] Öğüt S, Chelikowsky J R and Louie S G 1998 *Phys. Rev. Lett.* **80** 3162
[96] Öğüt S, Cheikowsky J R and Louie S G 1997 *Phys. Rev. Lett.* **79** 1770
[97] Shanno D F and Phua K H 1978 *Math. Program.* **14** 149
[98] Vasiliev I, Öğüt S and Chelikowsky J R 1999 *Phys. Rev.* B **60** 8477
[99] Troparevsky C, Kronik L and Chelikowsky J R 2002 *Phys. Rev.* B **65** 33311

[100] Schäfer R and Becker J A 1996 *Phys. Rev.* B **54** 10296
[101] Wang L W and Zunger A 1994 *J. Phys. Chem.* **98** 2158
[102] Schuppler S *et al* 1995 *Phys. Rev.* B **52** 4910
[103] von Behren J, van Buuren T, Zacharias M, Chimowitz E H and Fauchet P M 1998 *Solid State Commun.* **105** 317
[104] Kanemitsu Y *et al* 1993 *Phys. Rev.* B **48** 2827
[105] Lehmann V and Gösele U 1991 *Appl. Phys. Lett.* **58** 856
[106] Vasiliev I, Öğüt S and Chelikowsky J R 2001 *Phys. Rev. Lett.* **86** 1813
[107] Vasiliev I, Chelikowsky J R and Martin R M 2002 *Phys. Rev.* B **65** 121302
[108] Puzder A, Williamson A J, Grossman J C and Galli G 2002 *Phys. Rev. Lett.* **88** 097401
[109] Mitas L, Therrien J, Twesten R, Belomoin G and Nayfeh M H 2001 *Appl. Phys. Lett.* **78** 1918
[110] Vasiliev I and Martin R M 2002 *Phys. Status Solidi* b **233** 5
[111] Martin E, Delerue C, Allan G and Lannoo M 1994 *Phys. Rev.* B **50** 18258
[112] Takagahara T and Takeda K 1996 *Phys. Rev.* B **53** R4205
[113] Chelikowsky J R 2002 *MRS Bull.* **27** 951
[114] Alivisatos A P 1996 *Science* **271** 933
[115] Murray C B, Norris D J and Bawendi M G 1993 *J. Am. Chem. Soc.* **115** 8706
[116] Gorer S and Hodes G 1994 *J. Phys. Chem.* **89** 5338
[117] Gal D, Hodes G, Hariskos D, Braunger D and Schock H-W 1998 *Appl. Phys. Lett.* **73** 3135
[118] Kuno M, Lee J K, Dabbousi B O and Mikulec F V 1997 *J. Chem. Phys.* **106** 9869
[119] Carter A C *et al* 1997 *Phys. Rev.* B **55** 13822
[120] Soloviev V N, Eichhöfer A, Fenske D and Banin U 2001 *J. Am. Chem. Soc.* **123** 2354
[121] Wang L and Zunger A 1996 *Phys. Rev.* B **53** 9579
[122] Rabani E, Hetenyi B and Berne B J 1999 *J. Chem. Phys.* **110** 5355
[123] Deglmann P, Ahlrichs R and Tseresteli K 2002 *J. Chem. Phys.* **116** 1585
[124] Eichkorn K and Ahlrichs R 1998 *Chem. Phys. Lett.* **288** 235
[125] Troparevsky C, Kronik L and Chelikowsky J R 2003 *J. Chem. Phys.* **119** 2284
[126] Landoldt–Börnstein 1983 *Numerical Data and Functional Relationships in Science and Technology* (Berlin: Springer)
[127] Soloviev V N, Eichhöfer A, Fenske D and Banin U 2000 *J. Am. Chem. Soc.* **122** 2673
[128] Rogach A L, Koronowsky A, Gao M, Eychmüller A and Weller H J 1999 *J. Phys. Chem.* B **103** 3065